Spatio-temporal variation of radionuclide dispersion from nuclear power plant accidents using FLEXPART ensemble modeling

S. Omid Nabavi[1], Theodoros Christoudias[1], Yiannis Proestos[1], Christos Fountoukis[2], Huda Al-Sulaiti[2], Jos Lelieveld[1,3]

[1]Climate and~~&~~ Atmosphere Research Centre, the Cyprus Institute, Nicosia, 2121, Cyprus (o.nabavi@cyi.ac.cy)
[2]Qatar Environment and Energy Research Institute (QEERI), Hamad Bin Khalifa University, Doha, Qatar
[3]Atmospheric Chemistry Department, Max Planck Institute for Chemistry, Mainz, 55128, Germany

Correspondence to: ~~S. Omid Nabavi[1]~~Jos Lelieveld (jos.lelieveld~~o.nabavi~~@mpic.de~~cyi.ac.cy~~)

Formatted: Not Superscript/ Subscript

Commented [TCh1]: To waive publication fees

Abstract.

We ~~estimate~~ investigate the spatio-temporal distribution ~~the seasonal and diurnal changes~~ of radionuclides including Iodine-131 (^{131}I) and Cesium-137 (^{137}Cs), transported to Qatar from ~~a~~ fictitious ~~accident~~accidents at the upwind Barakah Nuclear Power Plant (B-NPP) in the United Arab Emirates (UAE). To~~For~~ model~~ing~~ the dispersion of radionuclides, we use the Lagrangian particle/air parcel dispersion model FLEXible PARTicle (FLEXPART) driven by forecasting and (re)analysis products, and additionally coupled with the Weather Research and Forecasting model (FLEXPART-WRF). A four-member ensemble of meteorological inputs, including one forecast dataset (~~CFSv2~~GFS) and three (re)analysis datasets (native resolution and downscaled FNL, and downscaled ERA5), is used to investigate the sensitivity of simulations to variations in meteorological inputs. We also investigate~~study~~ the sensitivity of the simulations to ~~accounting for~~ the skewness in the vertical velocity distribution. We ~~investigate~~ study the potential risk to populated areas from a nuclear accident in the ~~catchment~~ region of interest ~~(Qatar)~~. According to the simulated age spectrum of the Lagrangian particles, radionuclides enter southern Qatar about 20 to 30 hours after ~~the~~ release. Most of the radionuclide ~~transport and~~ deposition in the study area occurs within~~in less than 50 and~~ 80 hours after ~~the~~ release~~, respectively~~. A ~~higher~~ larger number of long-lived particles is found in the FNL-based simulations, which is interpreted as a greater dispersion of particles at~~into the~~ greater distance~~st~~ ~~part of the study area~~ from the emission ~~point~~location ~~in these simulations~~. The highest simulated ^{131}I concentrations and ^{137}Cs deposition show a pronounced spatio-temporal pattern. They are mostly found in the south/southeast of Qatar, during the early-daytime development of the boundary layer, and during the cold period of the year. The results show remarkable differences in the spatio-temporal distribution of ^{131}I and ^{137}Cs simulations based on the FNL and GFS datasets, which share a common basic meteorological model~~, although they produce the simulations with the highest agreement~~. We conclude that the variation of the meteorological inputs, downscaling~~the choice of the simulation code~~, and the turbulence scheme used under convective conditions can collectively lead to significant deviations in the radionuclide dispersion simulations. ~~The most populated areas of Qatar~~

~~coincide with moderate ^{131}I concentration and ^{137}Cs depositions while uninhabited areas in southern Qatar receive the highest amounts. Simulated concentrations are found with the same level of consistency as reported for real case studies.~~

1 Introduction

Modeling the spatiotemporal distribution of radioactive ~~materials~~compounds using chemical transport models ~~Modeling the spatio-temporal distribution of radioactive materials through chemical transport models~~ (CTMs), especially after large nuclear ~~events~~accidents, has received widespread attention ~~especially after major nuclear events, has received widespread attention~~ (Chino et al., 2011, Stohl et al., 2012, Christoudias and Lelieveld, 2013, Evangeliou et al., 2017). Whether explicitly stated or not, ~~all of~~ these studies aim to determine the extent and transport of radionuclides at various spatial scales. Thesey ~~studies~~ also aim to~~research activities help~~ improve the performance of CTMs, which are at the core of preparedness programs for potential nuclear accidents (or releases) associated with the growing number of nuclear facilities~~Whether explicitly stated or implied, all these studies seek to determine the magnitude and transport of radionuclides at different spatial scales. Such research activities help to improve the performance of CTMs as the core of preparedness programs for potential nuclear accidents (or releases) related to the increasing number of nuclear facilities~~ (Farid et al., 2017). However, case studies of ~~real~~large accidents, which typically cover ~~on the order of~~ a few days to a few weeks, are not suitable for studying the effects of diurnal and seasonal (atmospheric) changes on radionuclide dispersion, and the sensitivity to the meteorological (re-)analyses driving the simulations. ~~However, case studies of real accidents of the order of a few days are not suited to examine the impact of seasonal (atmospheric) changes on the radionuclide dispersion~~.

Maurer et al. (2018) found that the performance of dispersion models strongly depends on the successful modeling of boundary layer processes, which vary with season and time of day. Meteorological inputs to the CTMs are generated by atmospheric models, which may exhibit variability when simulating atmospheric conditions over nuclear accident areas (Arnold et al., 2015). ~~For example~~In addition, Long et al. (2019) studied the effects of the East Asian northeast monsoon on the transport of radionuclides from the Fukushima nuclear power plant accident to the tropical western Pacific and Southeast Asia. They found that in these regions, radioactivity levels are ~~is~~ lower than in other regions of the Northern Hemisphere, which is due to the late arrival of the radionuclide plumes carried by the monsoon circulations. That is, the dispersion of radionuclides from this accident could potentially be different under ~~any~~ other atmospheric conditions, which are only captured by the hypothetical, iterative simulation of this event at different times of the day and year. ~~On the other hand, Maurer et al. (2018) found that the performance of dispersion models strongly depends on the successful modeling of boundary layer processes, which vary with season and time of day. In term of local atmospheric conditions, In addition, meteorological inputs to the CTMs are generated by atmospheric models, which in some cases exhibit variability when simulating atmospheric conditions over nuclear accident areas (Arnold et al., 2015). This is mainly due to differences in initial conditions, spatial and temporal resolution, mathematical formulation, and physical parameterization.~~

While few new nuclear power plants are licensed in the Western world, and most Soviet-era stations are nearing the end-of-life decommissioning, ~~several~~new nuclear facilities are planned or proposed, and in the last few years are under construction or becoming operational in the Middle East/North Africa (MENA) region. The Barakah station is the ~~latest~~most recent NPP to become operational in a region with unique climatological conditions that were previously void of such developments and where the risk from radionuclide dispersion received little ~~coverage~~attention in the literature, ~~as opposed~~in contrast to Europe, Japan and the USA.

~~Using an ensemble of meteorological inputs, t~~

The main objective of this study is to investigate the spatiotemporal variability of radionuclide transport, surface concentration, and deposition after~~during~~ potential nuclear accidents, using an ensemble of meteorological inputs. Gaseous and aerosol~~Two~~ radionuclide~~active~~ tracers, ~~including~~ iodine-131 (^{131}I) and cesium-137 (^{137}Cs), are assumed to be released by a~~ina~~ fictitious ~~accident~~accidents at the Barakah Nuclear Power Plant (B-NPP) in the United Arab Emirates (UAE)~~. Both radionuclides are emitted as gases, but due to its lower volatility, ^{137}Cs condenses on aerosol particles shortly after release (Christoudias and Lelieveld, 2013)~~. The amount of ^{137}Cs that is deposited on the surface is important due to its relatively long half-life~~ of ^{137}Cs~~ (about 30 years), whereas the ^{131}I surface-level concentration (about 8 days half-life) is important for human health and~~in~~ the biosphere in the short term (Tsuruta et al., 2019, Pisso et al., 2019, Takagi et al., 2020, Kinase et al., 2020, Wai et al., 2020) ~~compared to ^{131}I (about 8 days), gives significance to the amount of ^{137}Cs that undergoes surface deposition and to ^{131}I concentration in the biosphere (Tsuruta et al., 2019, Pisso et al., 2019, Takagi et al., 2020, Kinase et al., 2020, Wai et al., 2020)~~.

Field Code Changed

Field Code Changed

For the dispersion modeling we use the Lagrangian particle model FLEXible PARTicle (FLEXPART) (Stohl et al., 1998, Stohl et al., 2005, Brioude et al., 2013). ~~The Eulerian CTMs model the transport of air pollutants by numerically solving the equation for the conservation of mass (Moussiopoulos, 1997, Zhang and Chen, 2007), which is computationally expensive (Brioude et al., 2013). Moreover, in an Eulerian model, a particle released from a point source loses its position in the grid-box (numerical diffusion)~~. Lagrangian particle dispersion models (LPDMs) instead ~~on the other hand~~ ~~have minimal numerical diffusion because they accurately~~ model the trajectory of each particle (Nabi et al., 2015), instead of modelling the transport of air pollutants by numerically solving the equation for the conservation of mass (Moussiopoulos, 1997, Zhang and Chen, 2007), ~~as is the case~~notably done with~~in~~ Eulerian CTMs (Brioude et al., 2013). ~~In addition,~~ LPDMs are computationally more efficient ~~for modeling particle dispersion because these models~~as they calculate advection and diffusion only for the location of each particle and not for the entire model domain. However, LPDMs also have ~~their~~ limitations~~s as well~~. They suffer from numerical errors in the interpolations of meteorological fields in space and time. In some cases, the particles may not remain well-mixed during simulation (Brioude et al., 2013). This is mainly due to the treatment of ~~because~~ ~~due to the lack of accuracy required to simulate~~ the stochastic motion of the particles ~~is not treated accurately enough~~ and/or ~~because~~ the mass balance of vertical velocity ~~is not very accurately mass balanced~~ with the horizontal winds. ~~, particles may not remain well-mixed during the simulation (Brioude et al., 2013).~~ Regardless of ~~which~~ the ~~type of CTM is~~ formalism used, Girard et al. (2016) have shown that uncertainties in meteorological fields, namely wind speed and direction and precipitation, and emission rate can contribute significantly to errors in dispersion modeling. According to Galmarini et al. (2004), ~~T~~there are three common methods for sensitivity analysis of LPDM simulations with respect to meteorological ~~information~~ fields ~~are~~: i) generating perturbations in the horizontal and vertical position of particles, ii) using a single meteorological model with perturbations in initial conditions and/or model physics, and iii) using a number of different meteorological models ~~(Galmarini et al., 2004)~~. By adopting the third approach, we ~~used~~ use a four-member ensemble in which the performance of the forecast member, forced by 6-hourly data from the Global Forecast System (GFS)~~NCEP climate forecast system version 2 (CFSv2)~~, ~~is~~ being compared to the members based (re)analysis datasets. ~~(Re)analysis-based simulations (unavailable in a real-world scenario) are expected to be closer to (unavailable in a real-world scenario) actual values than forecast-based simulations (Leadbetter et al., 2022).~~ Two members of the ensemble are forced by~~through~~ dynamically downscaled meteorological inputs to investigate the effects of downscaling ~~on FLEXPART~~to higher resolution i~~o~~n dispersion modeling. We also ~~studied~~ investigate the sensitivity of the simulations to the choice of turbulence schemes under convective conditions.

Finally, t~~T~~o study the potential risks to the local population, the radionuclide simulations ~~were~~ are examined in relation to the population density of the catchment region of interest (Qatar). To the best of our knowledge, this is the first time such a study has been conducted for potential radionuclide releases in the~~he study~~ region, and we anticipate that our results may contribute to the formulation of preparedness plans. The paper is organized as follows: section 2 describes the LPDM, meteorological inputs, study area, and source term of radionuclides used in this study. The results are presented and discussed in section 3. The conclusions of the study are presented in section 4.

2 Ensemble model configuration

~~We use FLEXPART and FLEXPART driven by the Weather Research and Forecasting model (FLEXPART-WRF) to model the dispersion of ^{131}I and ^{137}Cs fictitiously released from the B-NPP~~. A brief description of the FLEXPART modeling structure follows.

2.1 FLEXPART and FLEXPART-WRF dispersion modeling

We refer the reader to ~~The details of the modeling of FLEXPART and FLEXPART-WRF can be found~~ in ~~in~~Stohl et al. (2005)~~ Stohl et al. (2005), ~~(~~Pisso et al.~~,~~ (2019), and Brioude et al. (2013)~~, respectively~~ for detailed descriptions of the FLEXPART and FLEXPART-WRF models. Here~~In this subsection~~, only the principles of FLEXPART Lagrangian modeling are discussed to facilitate the presentation of the results in the next section. FLEXPART was developed as a LPDM based on the zero acceleration scheme (Eq. 1). It solves a Langevin equation (Eq. 2) to model the trajectories of Lagrangian particles. The new position of the particles is influenced by large-scale winds, local turbulence (stochastic component), and mesoscale motions.

$$X(t+\Delta t) = X(t) + v(X,t)\Delta t \quad (1)$$

$$\frac{dX}{dt} = v[X(t)]$$

where t is time, Δt is the time increment, X is the position vector, and $v = \bar{v} + v_t + v_m$ is the wind vector composed of the grid-scale wind $\bar{v}$, the turbulent wind fluctuations v_t , and the mesoscale wind fluctuations v_m. FLEXPART also quantifies changes in the mass, or mixing ratio, of transported particles~~(Stohl and Thomson, 1999)~~ carried away by calculating various removal processes ~~processes~~(Stohl et al., 2005, Grythe et al., 2017) ~~(Stohl and Thomson, 1999, Cassiani et al., 2015, Tipka et al., 2020)~~. Turbulent motions v_{t_i} for wind components i are parameterized assuming a Markov process based on the Langevin equation (Eq. 2).

$$dv_{t_i} = \alpha_i(x, v_t, t)dt + b_{ij}(x, v_t, t)dW_j \text{ (2)}$$

w~~W~~here α is the drift term, b is the diffusion term, and dW_j are incremental components of a Wiener process with mean zero and variance dt, that are uncorrelated in time (Stohl et al., 2010). The minimum value of Δt_i is 1 second. Δt_i is used only for the horizontal turbulent wind components of Equation 3.

$$\Delta t_i = \frac{1}{ctl} min(\Delta\tau_{L_\omega}, \frac{h}{2\omega}, \frac{0.5}{\frac{\partial\sigma_\omega}{\partial z}}) \text{ (3)}$$

where h is the height of the atmospheric boundary layer (ABL). To solve the Langevin equation for the vertical wind component, a shorter time step $\Delta t_\omega = \frac{\Delta t_i}{ifine}$ is used. Under convective conditions, when the turbulence is skewed, larger areas are occupied by downdrafts (instead of updrafts). This can lead to higher surface concentrations (deposition) in areas near pollution sources (Pisso et al., 2019). To investigate the sensitivity of radionuclide quantities to the turbulence scheme used, FLEXPART-WRF members ~~were~~ are re-run after replacing the standard Gaussian turbulence model (GTM) with the skewed turbulence model (STM) (Luhar et al., 1996, Cassiani et al., 2015). The results of these two schemes are used to calculate the vertical velocity component of the drift term in Eq. 2. The implementation of STM requires shorter time steps, dt in Eq. 2, to better resolve turbulence in the convective planetary boundary layer. Therefore, we ~~used~~ use ctl=10 and $ifine = 10$ as recommended by Brioude et al. (2013) and ~~a tenfold finer time step, as recommended by~~ Pisso et al. (2019), in sensitivity runs. For the computation of σ_{v_i} and $\Delta\tau_{L_i}$, FLEXPART uses the parameterization scheme proposed by Hanna (1982). To account for mesoscale motions, a method similar to that of Maryon (1998) is used.

In radionuclide dispersion modeling, particle mass reduction of occurs primarily through three processes~~processes~~: radioactive decay, dry deposition, and wet deposition. The following exponential equations characterize radioactive decay (Equation 4) and wet deposition (Equation 5).

$$m(t + \Delta t) = m(t)exp(-\Delta t/\beta) \text{ (4)}$$

where m is the particle mass and the time constant $\beta = \frac{T_{\frac{1}{2}}}{\ln(2)}$ is determined from ~~already calculated~~ the radionuclide half-life $T_{\frac{1}{2}}$.

$$m(t + \Delta t) = m(t)exp(-\Lambda\Delta t) \text{ (5)}$$

The scavenging coefficient Λ is calculated differently depending on whether the particles are in the aerosol or gas phase and whether the scavenging takes place inside or below the clouds (Stohl et al., 2005).

In this study, we ~~have used~~ use FLEXPART 10.4 and a modified version of FLEXPART 9.02 to input meteorological simulations from the Weather Research and Forecasting (WRF) model (Grell et al., 2005) (hereafter referred to as FLEXPART and FLEXPART-WRF, respectively). Compared to previous versions, FLEXPART has undergone a significant revision of the wet deposition calculation. The latest updates incorporate the dependence of wet deposition on aerosol particle size and precipitation type has been incorporated (Grythe et al., 2017). ~~In addition,~~ FLEXPART calculates wet deposition only for cloudy ~~pixels~~ grid cells where the precipitation rate exceeds 0.01 mm h^{-1}. Therefore, the accuracy of cloud pixel detection plays a critical role in the accuracy of the location and amount of wet deposition simulated by FLEXPART. In previous versions, ~~(~~including version 9.02 used in the development of FLEXPART-WRF 3.2~~)~~, in-cloud grid cells ~~were~~ are defined as ~~cells~~ those with precipitation and relative humidity above 80%. ~~and any~~ The grid cells below ~~grid cells~~ the in-cloud grid cells up to the surface are defined as below-cloud grid cells ~~beneath these grid cells as below-cloud ones~~ (Seibert and Arnold, 2013, Pisso et al., 2019). ~~Because of recent updates,~~ In recent updates to the FLEXPART's source code, the above threshold has been modified using the 3D cloud water mixing ratio (q_c) fields. The threshold of q_c ~~FLEXPART now uses 3D fields of cloud water mixing ratio~~ > 0 (q_c = 0) now identifies grid cells within the cloud (below the cloud) (Pisso et al., 2019). ~~and the relative fractions of ice and liquid water (type of precipitation).~~ Therefore, the differences in approaches in~~to~~ calculating scavenging between FLEXPART and FLEXPART-WRF may partially ~~it is expected that part of the~~ explain ~~difference~~ the ~~inconsistency~~ discrepancies between ~~of~~ ~~between the FLEXPART and FLEXPART-WRF~~ ~~resulting~~ simulations ~~in~~ for the wet season ~~is due to the differences in the schemes used to calculate the scavenging~~. Pisso et al. (2019) have discussed this and other updates in more detail in the latest version of FLEXPART. For dry deposition, for all particles below twice the reference height (h_{ref}), the reduction in particle mass is calculated using Eq. 6:

$$\Delta m(t) = m(t)[1 - exp\left(\frac{-v_d(h_{ref})\Delta t}{2h_{ref}}\right)] \quad (6)$$

v_d is the dry deposition velocity calculated as the ratio of $v_d(z) = \frac{F_C}{C(z)}$ for h_{ref} of 15 m. F_C and $C(z)$ ~~C~~ are the flux and concentration of a species at height z within the layer at constant flux. If the necessary information to parameterize of dry deposition of gases and particles is not available, v_d can be assumed to be constant. The concentration of a given gas or aerosol species in a grid cell is equal to the weighted average of the total particle mass within the grid cell divided by the volume of the grid cell (Pisso et al., 2019), as defined in Equation 7.

$$C(z) = \frac{1}{v}\sum_i^N (m_i f_i) \quad (7)$$

where V is the volume of the grid cell, m_i is the particle mass, N is the total number of particles, and f_i is the fraction (weight) of the mass of particle i assigned to the particular grid cell. The amount of dry and wet deposition ~~for~~ over the given grid cell ~~i~~ is accumulated by default over the time dimension of the output, unless the age composition of the air parcels is required, as ~~was~~ is the case in this study. A unique feature of FLEXPART/FLEXPART-WRF is the grouping of simulations based on the age of the Lagrangian particles. This means that the number of concentrations and deposition at each time step is obtained from aggregating the simulations over the additional dimension of particle age. In this study, we ~~used~~ use the age spectrum of Lagrangian particles to ~~estimate~~ investigate the age composition~~the transport~~ of radioactive materials from the source to the receptors. Air parcel ages are studied at an hourly resolution. As a result, the output grid, which has a horizontal resolution of 10 km and 14 vertical levels from 5 to 5000 m agl, gains an additional dimension with a length of 96 (hours). Thickness-weighted averages of simulated concentrations, hereafter referred to as near-surface concentrations, are calculated from concentrations within the bottom four model layers between 5 and 100 m agl (with layer thicknesses of 5 m, 5 m, 40 m, and 50 m). To statistically compare the age distributions of the ensemble members, we use the maximum normalized difference according to Equation 8. Assuming that a~~a~~ and b~~b~~ are two ~~of smooth density estimates of~~ air parcel age distributions that have been smoothed with the Gaussian kernel (Chung, 2020), their maximum normalized difference is calculated as the maximum value of the absolute differences between a and b divided by the maximum value of a and b. ~~(Chung, 2020)~~Larger variations in the distributions are indicated by higher values of this indicator (Jin and Kozhevnikov, 2011).

$$\text{maximum normalized difference} = \frac{\max(\mathrm{abs}(a-b))}{\max\,(\max(a),\max(b))} \quad (8)$$

~~Modeled concentrations are vertically integrated through all model levels in analyses related to air parcel ages (subsection 3.1) and inter-member evaluation (subsection 3.3). The thickness-weighted averages of simulations in the lowest four model levels between 5 and 100 m agl (with layer thicknesses of 5 m, 5 m, 40 m, and 50 m) are used for the spatial analysis (subsection 3.2).~~

Formatted: Centered

2.2 Meteorological data

FLEXPART and FLEXPART-WRF are driven~~work in the~~ offline by~~mode with~~ gridded meteorological fields from numerical weather prediction models~~ on a grid scale~~. In this study, we obtain meteorological products~~inputs~~ from the ~~NCEP climate forecast system version 2 (CFSv2~~GFS (NCEP, 2015a)~~) (Saha et al., 2011, Saha et al., 2014)~~, the NCEP final analysis (FNL) (NCEP, 2015b), and the ECMWF reanalysis fifth generation (ERA5) (Hersbach et al., 2020). ~~The CFSv2~~GFS ~~, which entered into the operational mode in March 2011,~~ is a fully coupled ~~climate~~ model that represents the interactions between oceans, land, and atmosphere. The ~~CFSv2~~GFS ~~can be~~dataset, available since 2015,~~ used to~~ provides 6-hourly forecast inputs at 03, 09, 15, and 21 hours~~ for FLEXPART~~ with a spatial resolution of 0.25 degrees~~onward~~. The FNL dataset is produced using the same base~~ic~~ meteorological model that produces the GFS dataset. The former provides the three-hourly combination of analysis (at 00, 06, 12, and 18) and forecast meteorological fields (at 03, 09, 15, and 21) at a spatial resolution of 0.25 degrees starting in 2015. ERA5 is the latest generation of ECMWF reanalysis data, covering the period from January 1, 1950 to ~~nearly~~ the present. It is ~~They are~~ generated in hourly time steps with a spatial resolution of about 0.25 degrees. ~~CFSv2~~GFS and FNL are used to force~~ the~~ FLEXPART directly. In addition, WRF 4.2 is applied to dynamically downscale the ERA5 and FNL to~~so that they can~~ be used as the input~~s~~ to FLEXPART~~downscaled members~~. They ~~are~~ are used~~then fed~~ in~~to~~ FLEXPART-WRF with higher downscaled ~~the new~~ spatial ~~and temporal~~ resolution~~s~~ of 10 km and hourly and temporal resolution~~, respectively~~. To the best of our knowledge, this is the first time that the ERA5 reanalysis has been used with the~~to~~ ~~implement~~ FLEXPART-WRF model setup. Table 1 provides an overview of the WRF model configuration.

Table 1 Overview of the WRF model configuration.

Dynamics	**Non-hydrostatic**
Initial and boundary condition data	FNL/ERA5
Temporal interval of boundary data	3 h/1 h
Resolution	10 km x 10 km
Extent of domain	17°N-33°N and 40°E-60°E
grid-nudging	On
PBL Scheme	YSU
Cumulus parameterization	Grell 3D ensemble scheme
Surface layer parameterization	Noah land surface scheme
Terrain and land use data	USGS

Table 2 provides an overview of the input data and the corresponding simulation codes. For comparison of the above meteorological inputs with observations, daily total precipitation and daily averages of wind speed and temperature data are obtained from 157 climate stations within the model domain. These observations are freely available from the Global Surface Summary of the Day (GSOD) database which is maintained by the National Oceanic and Atmospheric Administration (NOAA).

Table 2~~1~~ Summary of meteorological inputs used to run FLEXPART and FLEXPART-WRF.

Inputs	Simulation code	Spatial resolution	T~~t~~emporal resolution	T~~t~~ime coverage	D~~d~~ownscaled	T~~t~~ype of input	W~~w~~et deposition scheme
~~CFSv2~~GFS	FLEXPART~~_CFSv2~~	0.5 degrees	6-hourly	2011-present	~~X~~	forecast	Grythe et al. (2017)
FNL	FLEXPART~~_FNL~~/FLEXPART-WRF	0.25 degrees/ 10 km	3-hourly/ hourly	2015-present	~~X~~/✓	analysis	Grythe et al. (2017)/Seibert and Arnold (2013)
ERA5	FLEXPART-WRF	10 km	hourly	1950-present	✓	reanalysis	Seibert and Arnold (2013)

2.3 Emission scenario and study area

We ~~have simulated a~~simulate fictitious nuclear ~~accident~~accidents at the B-NPP (Fig. 1-A) in which 22 PBq (6.9 kg) of ^{137}Cs and 192 PBq (0.042 kg) of ^{131}I are released during the first 24 h of each 96-hour simulation period. These amounts are the upper bounds of emissions estimated by Babukhina et al. (2016) for the Fukushima Daiichi nuclear accident in ~~May~~ March 2011. Although ~~W~~we ~~simulated~~ simulate a fictitious release of radioactivity at a level comparable to the Fukushima nuclear accident~~. However,~~, our study does not intend to replicate past accidents or simulate~~s~~ a specific real-world case.~~;~~ These source terms are used ~~only because having~~to provide a real-world comparison that gives the reader a tangible point of reference.~~reference from which to make sense of the results.~~ ~~rather we designed this analysis to determine what time of the day and year is associated with particular probabilities of transport of dense radionuclide plumes from any hypothetical release in the study area.~~

The ~~optimal~~ number of Lagrangian particles required ~~for a given task~~ is dictated~~depends~~ by~~on~~ the specific problem at hand~~and needs~~ ~~To choose the optimal number of Lagrangian particles, we have followed the literature~~ (Papagiannopoulos et al., 2020, Thompson et al., 2015, Fast and Easter, 2006). The computational time scales increase linearly with the increasing number of particles, while the statistical error of the simulations decreases with the square root of the particle density (Pisso et al., 2019). In this study, a~~A~~ total number of 10^4 Lagrangian particles ~~were~~ are released ~~almost~~ uniformly during the emission period ~~(~417 particles per hour)~~. To assess~~test~~ if this rate ~~number of particles~~ is sufficient, we ~~to~~ study the dry deposition process, which is directly influenced by the boundary layer conditions.~~,~~ W~~w~~e performed a preliminary test run with GFS data with a 10-fold increase in particles. As shown in S1, the simulated dry deposition of ^{137}Cs and ^{131}I and the wet deposition of ^{137}Cs do not undergo significant changes with the increase ~~in particles~~of an order of magnitude.

Regarding the height of the releases, ~~This result shows the sufficiency of the particle abundance to study the transport and deposition of particles near the surfaceTo choose the optimal number of particles, we have followed the literature (Papagiannopoulos et al., 2020, Thompson et al., 2015, Fast and Easter, 2006). The computational time scales linearly increase with the increasing number of particles, while the statistical error of simulations decreases with the square root of the particle density (Pisso et al., 2019). T~~the particles are ~~initially distributed~~emitted at ~~height~~ model ~~heights~~ levels between 100 and 300 m above ground level (agl) above~~t~~ the emission point. Each simulation starts at the beginning of each day and lasts 96 hours (Fig. 1-B). We ~~This experiment has been~~ run this scenario~~ed~~ for every day of the year 2019, resulting in a total of 1460 simulation days (365 days of the year x 4 forward simulation days). In the following analysis, w~~W~~hen reporting particle ages associated with the simulations~~For the diurnal and seasonal stratification of simulations~~, we always refer to the time when a particle is released ~~(not to when it travels or reaches receptors)~~. The simulation domain extends~~is limited~~ between 17°N-33°N and 40°E-60°E, ~~17°N-33°N and 40°E-60°E,~~ and for post-processing ~~the~~ we analyze simulations ~~geographical box~~ over Qatar, between ~~from~~ 24.25°N~~- to~~ 26.35°N and ~~from~~ 50.65°E~~- to~~ 51.75°E~~, has been analysed~~.

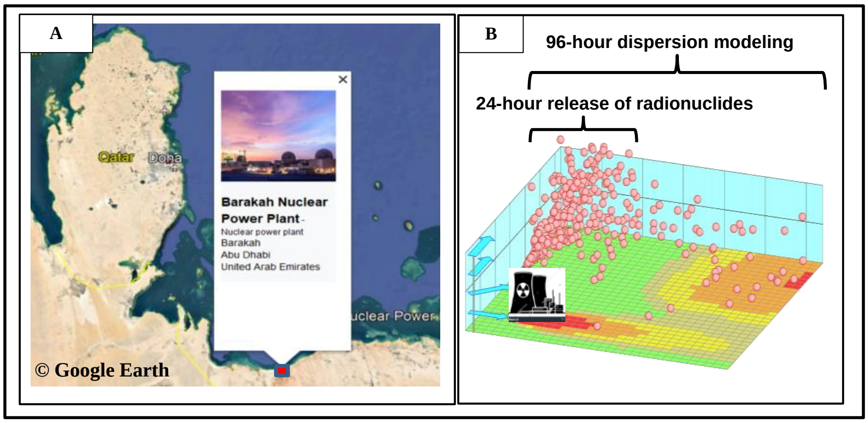

Figure 1 A: Study area encompassing the B-NPP (red square) and the State of Qatar. The base map and overlay information are from Google Earth. B: Schematic representation of the LPDM simulation cycle. The original image is~~A is the study area embracing the B-NPP (red square) and the state of Qatar. The base map and overlaying information are taken from Google Earth. B is the schematic illustration of the LPDM simulation cycle. The original figure is~~ available at https://www.janicke.de/en/lasat.html (last accessed: ~~4 October~~ February 1, ~~2022~~2023).

3 ~~FLEXPART/FLEXPART-WRF simulations~~Results and discussion~~:~~

3.1 Meteorological inputs vs. observations

~~In this section,~~ W~~we~~ compare the relevant meteorological input fields~~s~~ including daily mean surface wind speed and temperature and daily total precipitation with observations from 157 ~~climate~~ stations spanning~~within~~ the model domain (Fig. 2).

A relatively ~~The~~ large~~rst~~ discrepancy between observations and model inputs is ~~observed~~attained for precipitation~~In this section, we compare the daily average of surface wind speed and temperature and total precipitation with observations measured in climate stations within the model domain.~~. ~~The highest inconsistency with observations was found in precipitation simulations (red dots in figure 1). The used datasets yielded~~The average~~d~~ Spearman correlation coefficient (r) of ~~about~~ ~0.41 and root mean square error (RMSE) of 3.5 indicate a moderate relationship between precipitation inputs and observations in all members ~~a Spearman correlation coefficient of about 0.4 (with the highest in ERA5-WRF) and a RMSE of 3.5 (with the lowest in FNL dataset).~~ The ERA5-WRF and FNL datasets have the highest correlation (0.44) and lowest RMSE (3) compared to~~with~~ observations. All datasets, especially the downscaled ones, underestimate precipitation amounts, resulting in an average~~d~~ mean bias error (MBE) of -0.22~~All datasets, especially downscaled ones, underestimated precipitation amounts.~~ ~~This is to be expected since P~~precipitation is the result of complex sub-grid-scale processes, most of which are parameterized in atmospheric models~~, and it suffers from the multiplicative effect of errors in thermodynamics and dynamics~~. ~~This is to be expected as precipitation results from complex processes that are mostly parametrized in atmospheric models and it suffers the multiplicative effect of errors in both thermodynamics and dynamics.~~ Furthermore, precipitation can be spatially inconsistent due to ~~the~~ complex topography of the study area~~In addition, in contrast with the variables such as temperature and wind speed, precipitation can be spatially patchy due to presence of complex topography~~ (Tapiador et al., 2019).

All meteorological datasets are close~~r~~ to the observations when evaluating the simulations of wind speed and temperature (S2).~~All datasets are found much closer to observations considering the simulations of wind speed (Fig. 1) and temperature (S1).~~ The ERA5-WRF dataset shows the best agreement with the wind speed observations in terms of correlation (0.65) and RMSE (1.5), but ~~. However, this dataset underestimates the~~underestimates wind speed ~~more~~ to a greater extent~~d~~ than the GFS and FNL datasets. All datasets are significantly~~well~~ correlated with the temperature observations and with each other, as shown by the distribution of data points along the identity line. ~~The ERA5-WRF dataset yielded the highest agreement with wind speed observations, in terms of correlation (0.65) and RMSE (1.5). However, it has underestimated the wind speed more than GFS and FNL datasets. Regarding the air temperature, as expected, all datasets are well correlated with observations and with each other indicated by a fair distribution of the data points along the unity line.~~ From these~~e above~~ results, we~~it can be~~ conclude~~d~~ that the downscaled datasets ~~have relatively better performance in terms of~~ correlate better~~ion~~ with observations~~.~~ ~~However, this comes~~ at the ~~cost~~expense of an increase in error and bias values, especially for the wind speed~~ simulations~~.

I~~The i~~ntercomparison of the input datasets shows that the FNL and GFS simulations have the ~~highest~~best agreement, as can be expected since they are produced using the same data assimilation and forecasting system.~~According to the above results, it can be concluded that the downscaled datasets have a relatively better performance in terms of correlation with observations. However, the increase in their association with the observations has come at the price of increase in the error levels, especially in wind speed simulations.~~ However, we keep both datasets for the ensemble analysis because the smallest difference in the meteorological input leads to sequential deviations in the transport of air pollutants, as will be shown later.~~It is worth to notice that the mere comparison of meteorological inputs against surface observations is not adequate to identify the best meteorological dataset for the modeling of radionuclide dispersion (and it is not the purpose of this study either). We only have access to daily meteorological data at surface at a few points whereas transport modeling is carried out in several layers of the atmosphere in hourly time step throughout the study area. In addition~~ ~~The inter-comparison of datasets shows that FNL and GFS simulations have the highest agreement because they are products from the same data assimilation and forecast system. However, we decided to use both datasets for the ensemble analysis on the grounds that subtle differences in meteorological~~

~~inputs can have additive impacts on transport and distribution of air pollutants, discussed later.~~ The ~~relatively higher~~better agreement found between the ERA5-WRF and FNL-WRF datasets than between the latter and the FNL dataset shows the impact of the downscaling on the homogeneity of the meteorological inputs. ~~The relatively higher agreement of ERA5-WRF with FNL-WRF dataset than with FNL dataset indicated the increased homogeneity of two global scale-scale datasets due to dynamical downscaling.~~ It should be noted~~, although this is not the goal of this study.~~ that a systematic~~simple~~ comparison of meteorological datasets with ~~sporadic~~a representative sample of surface observations is ~~not~~ needed~~sufficient~~ to determine the optimal choice of~~best~~ meteorological inputs for forcing a CTM for different regions. ~~In addition,~~Here we have access to daily surface meteorological data, while transport modeling is performed in several layers of the atmosphere at hourly timesteps or ~~finer~~shorter.~~, in cases where the forecast of radionuclide dispersion is of interest, not many forecast datasets, like GFS, are left to choose for making a forecast run.~~

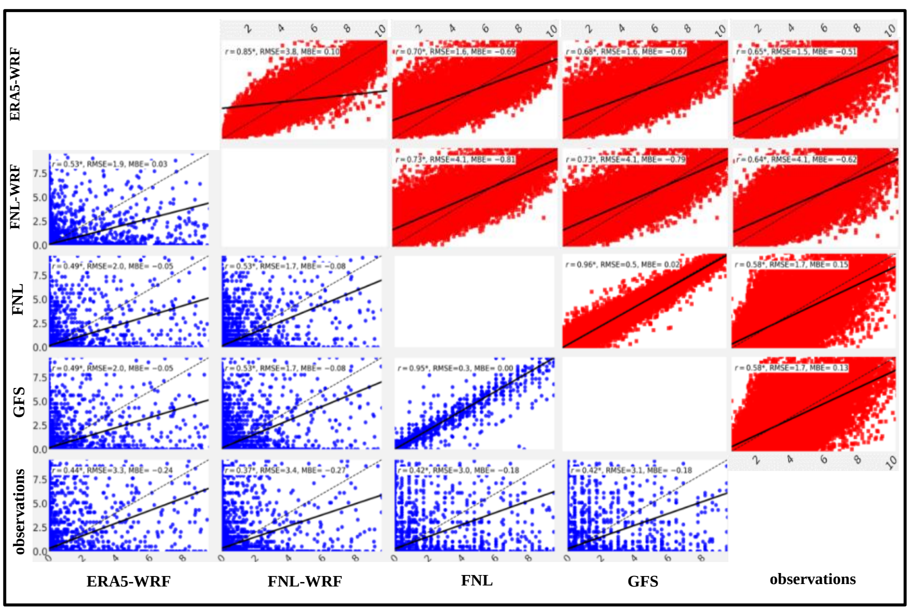

Figure 2 Scatter plot of observed daily total precipitation (mm, shown as blue circles) and daily mean wind speed (m/s, shown as red squares) against FLEXPART/FLEXPART WRF inputs. The scatter plot of observed and simulated daily surface temperature (k) is shown in S2. The observations are obtained from 157 climate stations in the study area~~Scatter plot between observed daily total precipitation (mm, shown in blue circles) and daily average of wind speed (m/s, shown in red squres) and FLEXPART/FLEXPART-~~

~~WRF inputs. The scatter plot of daily surface temperature (k) is shown in S1. Observations are obtained from 157 climate stations in the study area~~.

3.2~~1~~ Age composition of radionuclide plumes

~~It should be noted that due to high solubility and the relatively long half-life of ^{137}Cs, further emphasis is placed on the spatio-temporal distribution of ^{137}Cs deposition. Conversely, the ambient surface-level concentration of ^{131}I over the study area will be considered since it resides mostly in the gaseous phase and has a short half-life of 8 days.~~

~~In order to investigate the diurnal and seasonal variations in the transport of radionuclides, we examined the simulated age of the Lagrangian particles entering the study area by the season and time of day in which they were released from B-NPP.~~ The seasonal distributions of the air parcel ages for ^{131}I and ^{137}Cs are shown in Figures 3 and S3, respectively. The high degree of ~~significant~~ similarity between~~of~~ the age distributions of ^{131}I and ^{137}Cs is due to the fact that the removal process in LPDMs only affects mass concentrations and ~~does~~ not ~~affect~~ particle positions~~, but masses~~. ~~indicates that differences in the transport characteristics of these radionuclides, such as the wet and dry deposition rate and radioactive decay, are not large enough to cause the abundance of cases where ^{131}I and ^{137}Cs particles are not present in a common grid. The close dispersion of ^{131}I and ^{137}Cs concentrations, especially at low intensities, and, consequently, the age of corresponding air parcels can be attributed to the lack of heavy precipitation in the region. This can be seen in S2 where a positively skewed distribution is found for the ratio of ^{137}Cs wet deposition to total ^{137}Cs deposition.~~ Therefore, the following discussion of the ages of the ^{131}I particles is also valid for the ages of the ^{137}Cs ~~concentrations~~ particles (shown in the supplement). All ensemble members, in particular ~~especially~~ GFS and FNL~~, in fall,~~ ~~in all seasons~~ simulate predominantly~~an abrupt increase (or a peak) in the number of~~ air parcels with lifetimes of less than 20 to 30 hours in the autumn season~~in all seasons~~. ~~This indicates that, in most cases,, the regardless of the time of year, radionuclide clouds begin to cross the boundaries of the study area within a few hours after the emission~~. Other than~~Except for~~ fall, ~~where the GFS and FNL have a stronger peak in the above time interval,~~ the age distribution of the particles is relatively similar in all other seasons. As ~~will be~~ discussed in the ~~sub~~section 3.2~~, the frequency of radionuclide transfer to the study area in all ensemble members is much lower in fall than in winter and spring. Therefore, we believe that~~ a seasonal~~n unusual~~ atmospheric pattern simulated in the GFS and FNL datasets is responsible for the ~~striking~~ difference in particle age distributions in fall. Compared to the other ensemble members, the FNL-based simulations show a~~the most~~ delayed appearance of the second peak in air particle ages. This could be due to ~~1-~~ a decrease in transport speed to the same receptors and/or ~~2-~~ a higher number~~frequency~~ of air parcels reaching areas away from the source (discussed later). ~~The maximum normalized distance of age distributions (Fig. 3) shows larger similarity between FNL-WRF and ERA5-WRF than between the former and FNL in all seasons other than the fall (0.3, 0.19, 0.25, and 0.38 vs. 0.3, 0.32, 0.32, and 0.41 in fall, spring, summer, winter). This may to be due to the use of meteorological inputs with the same spatio-temporal resolution and a common simulation code and, consequently, similar modeling schemes for the two former members. Although the base model used for the production of FNL, the Global Forecast System (GFS), is also the atmospheric component of CFSv2, the distribution differences were found to be lower between the FNL age distribution and those from ERA5- and FNL-WRF for~~

~~most seasons. In addition to having finer spatial resolution than CFSv2, FNL assimilates observations like ERA5. Compared to other members, air parcel ages are distributed in a wider range in all seasons in FNL (note the location of the first and last peaks). This could be because: FNL simulated 1- a decrease in transport speed to the same receptors and/or 2- a higher frequency of air parcels reaching further receptors from the source (discussed later).~~

To understand how ~~the~~ radionuclide concentrations ~~transport~~ may vary with transport times~~with the level of radionuclide concentrations~~, ~~beside the previous categorization,~~ air parcel ages ~~were~~ are divided into three groups~~levels~~ ~~representing~~ corresponding to low (the top row in S4~~-A~~), moderate (the bottom row in S4~~-A~~), and high (the bottom row in Fig. 3~~-A~~) ~~concentrations~~ near-surface concentrations of ^{131}I (see S3 and S5 for ^{137}Cs). These categories are determined for each member based on ~~on column (mass) densities, computed from the vertical integration of concentrations. The low, moderate, and high~~ concentrations~~values~~ below the 33rd percentile, between the 33rd and 66th percentiles, and above the 66th percentile, ~~are~~ respectively. The ~~short time interval required for the~~rapid transport of dense radionuclide clouds within the region of interest~~to the study area~~ is demonstrated by the strongly ~~positively~~ skewed age distributions of particles corresponding to moderate and high radionuclide concentrations in all members and all seasons. ~~Given the proximity of the source (B-NPP) to the southeast of the study area, these results are expected.~~ The variation~~dissimilarity~~ of ~~the~~ age distributions for high and moderate concentrations in summer can be attributed ~~to the low frequency of radionuclide transfer to Qatar and~~ to an unusual transport pattern in this season ~~(as what observed for the air parcel ages corresponding to all concentrations in fall)~~.

It is ~~also~~ worth noting that all members of the ensemble ~~model (including the forecast member)~~ have a greater agreement for air parcel ages corresponding to the moderate and high levels of ^{131}I and ^{137}Cs concentrations than for those corresponding to low ~~concentrations~~concentrations. This is consistent with the principles of FLEXPART dispersion modeling. According to Pisso et al. (2019), the error rate of the simulations decreases with the square root of the particle density. As a result, all four members simulate the age of Lagrangian particles corresponding to moderate and high concentrations in better agreement~~more closely~~ and~~, most~~ likely~~,~~ more accurately near the source. ~~The age distributions corresponding to the low concentrations are almost the same as those corresponding to all concentrations.~~ Using the maximum normalized distance, a~~the~~ quantitative comparison of the particle age distributions, corresponding to all concentrations, is shown in Figure 4. The age distribution in the ERA5-WRF- and FNL-WRF-based simulations shows a greater similarity than to that of the FNL-based simulations in all seasons, except fall. This is due to the ~~use of~~ dynamic~~ally~~ downscaled meteorological inputs with the same spatio-temporal resolution ~~and to a common simulation code for ERA5- and FNL-WRF~~. The age distributions based on the FNL and GFS inputs, which are generated by a similar base model, do not show the same degree of similarity in all seasons. They have the smallest difference in fall and spring and ~~the greater~~a larger difference~~but not~~ in winter and summer, ~~where the distance between the age distributions based on~~contrary to ~~the~~ intercomparing FNL and FNL-WRF ~~datasets is the smallest~~. ~~Figure 2-B (S1-B) shows the categorization of age distributions based on the release time of particles carrying ^{131}I (^{137}Cs) in the first 24~~

~~hours of each simulation period. This panel is similar to 2-A, but shows the age distributions plotted separately for particles released in 6-hour periods of the first day of the simulations. For example, the upper left figure shows the age distribution of the particles that is released within the first 6 hours of simulations. This new categorization reveals that the number of long-lived air parcels (including all intensities of concentrations) increased in all members when particles are released between 12 and 6 p. m. (top row in Fig. 2-B and S1-B). This temporal pattern may be due to the coincidence of particle release and the development of the planetary boundary layer in the afternoon that caused the transport of radionuclides to longer distances, represented by longer Lagrangian particle ages. Because particles that are released at the end of the day have less time to travel by the end of simulation period, a sharper fall is observed in the right tail of the age distributions during the second half of the day. However, the lifetime of most simulated particles, especially of those that caused moderate (bottom row in Fig. S3-B and S4-B) and high intensities (bottom row in Fig. 2-B and S1-B), is found to be between 20 and 70 hours after release. Consequently, the difference in release time of Lagrangian particles is not significantly affected by their age spectrum. Compared to ERA5-WRF and FNL-WRF, CFSv2 and FNL have simulated a larger number of shorter-aged air parcels after sunset (between 6 and 11 p.m.). It is because the spatio-temporal resolution of inputs used in these two members is too coarse to resolve the gradual reduction of boundary layer height resulting in fewer particles being transported to remote areas.~~

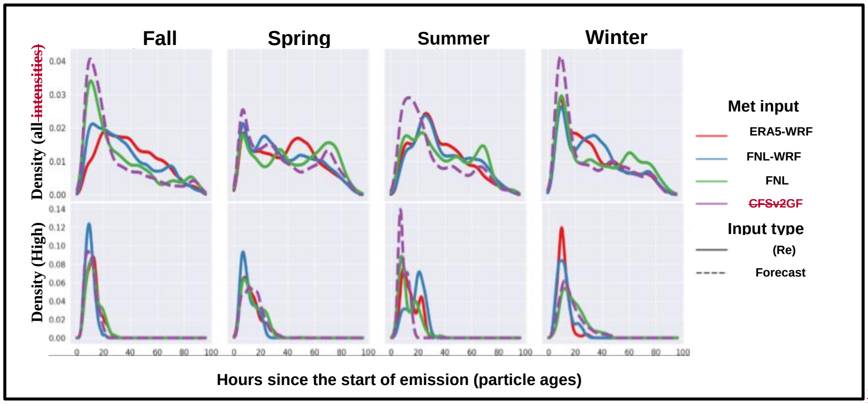

~~Like seasonal distribution, the diurnal variations of air parcel ages for high concentrations are very similar in all members. They all simulated a higher number of shorter-lived parcels when they are released in the first half of the day. Although a firm conclusion would require further studies at very-high-resolution of land-sea circulations in the region, onshore winds passing the emission point from the south may cause the abundance of shorter-lived parcels in southern Qatar.~~

Figure 3 A: ~~Smoothed age~~ D~~d~~istributions of the air parcels corresponding to all ^{131}I ~~intensities~~ concentrations ~~of ^{131}I column densities~~ (top row) and of those above the 66th percentile (bottom row). ~~B: the same as A, but for four times of the day. The curves represent simulations from each member of the ensemble.~~ y-and x-axes show density values and air parcel ages, respectively.

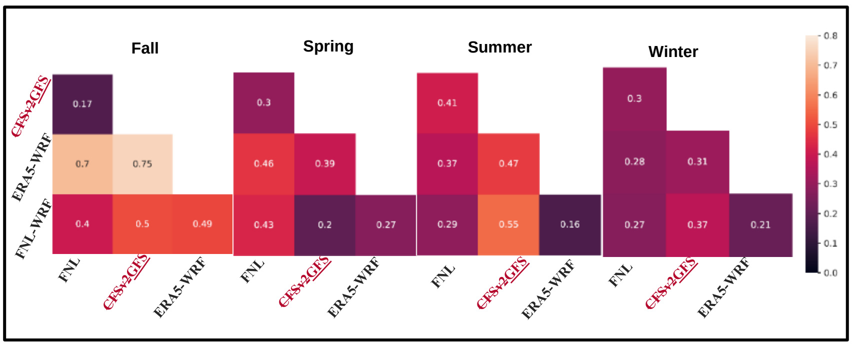

Figure 4 Seasonal maximum normalized difference of air parcel age distributions.

Due to the relatively long half-life of ^{137}Cs, its deposition rate in the affected areas is of great importance. To analyze the relationship between the age composition of air parcels and the amount of ^{137}Cs deposition, the deposition values cumulatively aggregated across time steps (~~j~~j) and age spectra ~~a~~ (~~i~~i) are normalized to the total amount of ^{137}Cs deposition ~~simulated~~ in each grid cell (k) at the end of each simulation run (l).

$$\cancel{{}^{137}\mathrm{Cs}_{klta_{norm\_depso}} = \begin{cases} \frac{\sum_{i=1}^{a} {}^{137}\mathrm{Cs}_{klij}}{\sum_{j=1}^{96}\sum_{i=1}^{96} {}^{137}\mathrm{Cs}_{klij}} & if\ j = 1 \\ \frac{\sum_{j=1}^{t-1}\sum_{i=1}^{96} {}^{137}\mathrm{Cs}_{klij} + \sum_{i=1}^{a} {}^{137}\mathrm{Cs}_{klij}}{\sum_{j=1}^{96}\sum_{i=1}^{96} {}^{137}\mathrm{Cs}_{klij}} & if\ j > 1 \end{cases}} \quad \cancel{(9)}$$

$${}^{137}\mathrm{Cs}_{klna_{norm\_depso}} = \begin{cases} \frac{{}^{137}\mathrm{Cs}_{kl(n-1)n}}{\sum_{j=1}^{96}\sum_{i=1}^{95} {}^{137}\mathrm{Cs}_{klij}} & if\ n = 2 \\ \frac{\sum_{j=1}^{n-1}\sum_{i=1}^{j-1} {}^{137}\mathrm{Cs}_{klij} + \sum_{i=1}^{a} {}^{137}\mathrm{Cs}_{klin}}{\sum_{j=1}^{96}\sum_{i=1}^{95} {}^{137}\mathrm{Cs}_{klij}} & if\ n > 2 \end{cases} \quad (9)$$

where n is the time step with a maximum of 96 (the last time step) and a is the given particle age with a maximum of n-1. ${}^{137}\mathrm{Cs}_{klij} = 0$ in two conditions (1) $n >= 26$ if $i \in [1, n - 25]$ and (2) $i >= j$.

Figure 5 shows the normalized deposition amounts (${}^{137}\mathrm{Cs}_{kln\cancel{t}a_{norm\_depso}}$) in winter, when both dry and wet deposition occur in the study area. ~~It is worth noting that~~ S~~s~~imilar deposition patterns are obtained~~seen~~ for~~in~~ other seasons (S6). As shown in S7, the main reason for the small difference between the seasonal deposition patterns is the lack of precipitation and subsequent wet deposition in the region. Although the spatial pattern of the deposition varies considerably, as indicated by the range of quartiles, the median of the normalized deposition shows that about 80 percent of the deposition occurs within 80 hours after an~~the hypothetical~~ accident~~s~~. The ~~fall in the~~ cumulative deposition at the end of the simulation period is mostly in~~related to~~ the areas farthest~~ar~~ from the source, and~~but~~ the total deposition reaches 100% as it approaches the end of the 96-hour simulation period. This is ~~clearly~~ evident~~can be better understood~~ in S8, where the ages of the deposited particles ~~simulating the ^{137}Cs deposition~~ peak around 20-30 hours, with~~and~~ a rather small number ~~of them are older than~~after 80 hours.

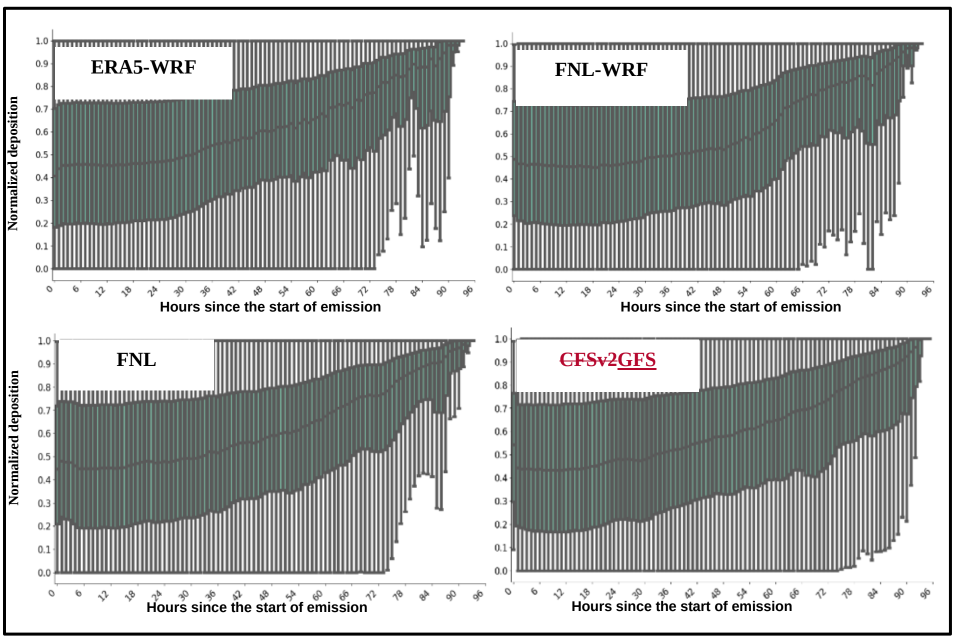

Figure 5 T~~t~~he normalized cumulative ^{137}Cs deposition to the total ^{137}Cs deposition of ~~amount~~ each 96-hour simulation period at each grid cell in winter. ~~This~~ Results for other seasons are shown in S6. ~~plot (S5) shows simulations in winter (other seasons).~~ The x-axis shows the age of the Lagrangian particles and the y-axis is the normalized deposition. The boxes show the quartiles of the normalized deposition. The whiskers represent the range between 1.5 times the interquartile range above the upper quartile and below the lower quartile.

3.2 Spatio-temporal distribution of radionuclides

For the analysis of near-surface radionuclide concentrations, the height~~thickness~~-weighted average ~~of the simulations~~ in the bottom four layers of the model between 5 and 100 meters agl ~~has been~~is used. ~~Because of the high radioactivity of ^{131}I and the solubility and relatively long half-life of ^{137}Cs, we focus in this part on ^{131}I concentrations and ^{137}Cs deposition. In view of the serious health risks, including thyroid cancer, that the exposure to ^{131}I radiation may cause (National Research Council, 1999), Using the model proposed by WHO (2012) for internal dose from inhalation,the seasonal median of the 96-hour integrated ^{131}I concentrations ($^{131}I^{intg_conc_seas}$, (in units of Bq m^{-3}) is converted to the thyroid internal dose from inhalation effective dose from inhalation of ^{131}I (TIDI, in units of µSv) (WHO, 2012),. The model conversion coefficients inputs are as specified defined by by WHO (2012) for three age groups: 1-year-old-infants, 10-year-old children, and adults (11 years and older). Considering thatSince approximately 90% of the population of Qatar is in the adult age group (UNStats, 2020), the inhalation doses calculated for this age group are discussed here (Fig. 6) and those for two others are available in the supplement (Figures S7 and S8). As reference values for comparison, TIDI values between about 2000 and 20000 µSv are measured in the first year following the Fukushima accident in areas close to the emission point (see Table 4 in WHO (2012)). The ensemble simulations show that the largest advance of TIDI above 2500 µSv into the study area occurs in the cold period of the year, especially in fall, in the simulations of all members. This may be due in part to the lower (higher) PBLH in the cold (warm) seasons and to the synoptic patterns that bring the radionuclides into the study area. An exception to this rule, however, is the distribution of TIDI in the FNL-based simulations during the summer. It appears that an unusual weather pattern caused abnormal TIDI values to occur in central Qatar during the summer. This may change as the modeling period is extended. In terms of spatial distribution, the TIDI above 2500 µSv occur close to the source in the southeastern part of the study area, and the intensity of the TIDI decreases with increasing distance to the north of Qatar. In other words, southeastern Qatar is the first area to be affected by dense ^{131}I clouds in the event of a a nuclear accident, especially during the cold period of the year. The comparison of the TIDI simulations between the members of the ensemble shows that, despite the similarities mentioned above, there are also clear differences. The advance of TIDI above 2500 µSv to the southeast of Qatar in simulations based on FNL inputs occurs in both fall and winter, but is observed only in winter in the GFS-based simulations. TIDI values peak in the fall in both downscaled runs, with inputs from the ERA5- and FNL-WRF datasets, but the extent of high TIDI values to the southeast of Qatar in fall is much larger in the ERA5-WRF run. This is also true when comparing the FNL-WRF and FNL-based simulations. The above-mentioned differences between the members have resulted in TIDI values varying by a factor of 2 to 10 in the south of Qatar.~~ To investigate the influence of the particle release time on the radionuclide dispersion, the seasonal median of the particle release time (hours in local time (LT)) coinciding with the maximum concentration of ^{131}I and the completion of ^{137}Cs deposition is considered (contours in Figures 6 and 7). ~~To identify the highest possible level of pollution at each point, regardless of its frequency, local maxima are calculated only from non-zero intensities.~~ The results show that the highest ^{131}I concentrations ~~is~~ coincide with particles released between 9 a.m. and 2 p.m. LT in most parts of the study area. This is the time of day when the development of the planetary boundary layer, the intensification of the land-sea thermal gradient, and the resulting daytime onshore winds coincide in the region. Among the members, the earliest particle release times (between 6 and 9 a.m. LT) leading to the highest ^{131}I concentrations are observed in simulations based on ERA5-WRF data. ~~On the contrary~~In contrast, it can be seen that the particles released after 6 p.m. LT lead to the highest concentrations in the vicinity of B-NPP in the southeast ~~of Qatar in the simulations~~ based on GFS and FNL~~ datasets~~, especially in fall. This can be attributed to the decrease in boundary layer height at this time of day~~, which leads to an increase in radionuclide concentrations in areas close to the accident site~~.

Figure 7 shows the seasonal median of total ^{137}Cs deposition (^{137}Cs^{tot_depos_seas}) simulated by four ensemble members. As defined by the International Atomic Energy Agency (IAEA, 2009), any area covered by radioactive substances that emit beta particles and gamma rays, such as ^{131}I and ^{137}C, in quantities greater than 40 kBqm^{-2} is considered to be "contaminated". ~~Accordingly, all~~Accordingly, all members have simulated deposition above this threshold over a significant portion of the study area during the cold period of the year. ~~As with TIDI, t~~The highest ^{137}Cs^{tot_depos_seas} are observed in the south and southeast~~, of Qatar~~ near the emission point. Compared to the FNL- and GFS-based simulations, the simulations based on the FNL- and ERA5-WRF datasets show the much greater extent of the contamination of the ^{137}C deposition over almost the whole of Qatar in the winter and, to a lesser extent, in the fall. Among the ensemble members, the highest ^{137}Cs^{tot_depos_seas} in the southeast~~ of Qatar~~ are seen in the simulations based on ERA5-WRF inputs, followed by the FNL-WRF-based simulations, in fall. While the ERA5-WRF-based simulations of ^{137}Cs^{tot_depos_seas} exceed 300 kBqm^{-2}, the deposition in GFS-based simulations is~~are~~ up to ten times lower at the same location and same period. The ^{137}Cs^{tot_depos_seas} in the warm period of the year, except for the simulations based on the FNL dataset in summer, are mostly either close to or below the threshold. The higher ^{137}Cs^{tot_depos_seas} in the cold period of the year, especially in winter, can be largely attributed to the seasonal increase of ^{137}Cs transport by northerly winds, discussed later, and to the relative increase in wet deposition (S7). The above results indicate that if a nuclear accident occurs during the cold period of the year, the magnitude of extreme ^{131}I concentrations and total ^{137}Cs deposition in the south of Qatar may be up to 10 times greater than during the warm seasons. A similar order of magnitude~~ is seen~~ in simulated variability is seen across the ensemble members. With respect to the particle release times, ^{137}Cs^{tot_depos_seas} occur mainly when particles are released between 10 a.m. and 5 p.m. LT, in the presence of a turbulent boundary layer. The analysis of the age spectra in subsection 3.2 shows the higher frequency of long-lived air parcels in the FNL-based simulations (see top row in Figure 3).

In view of the serious health risks, including thyroid cancer, ~~that~~which can be caused by the exposure to ^{131}I radiation~~ may cause~~ (National Research Council, 1999), the seasonal median of the 96-hour integrated ^{131}I concentrations (^{131}I^{intg_conc_seas}, in units of Bq m^{-3}) is converted to the thyroid internal dose from inhalation (TIDI, in units of μSv). We use the coefficients defined by WHO (2012) to calculate dosages for three age groups: 1-year-old infants, 10-year-old children, and adults (11 years and older). Since approximately 90% of the population of Qatar is in the adult age group (UNStats, 2020), the inhalation doses calculated for this age group are discussed here (Fig. 6). As reference values for comparison, TIDI values between about

Formatted: Superscript

Formatted: Superscript

2,000 and 20,000 µSv weare measured in the first year following the Fukushima accident in areas close to the power plant (see Table 4 in WHO (2012)). Our ensemble simulations show that the largest TIDI above 2500 µSv occurs in the cold period of the year, in fall, in the simulations of all members. This may be due in part to the lower (higher) PBLH in the cold (warm) seasons and to the synoptic conditions. An exception is the distribution of TIDI in the FNL-based simulations during the summer. This may change as the modeling period is extended. In terms of spatial distribution, the TIDI above 2500 µSv occur close to the source in the southeastern part of the domain, and the intensity of the TIDI decreases with distance to the north. Southeastern Qatar is the first area to be affected by dense ^{131}I clouds in the event of a nuclear accident, especially during the cold period of the year~~.~~. The advance of TIDI above 2500 µSv to the southeast of Qatar in simulations based on FNL inputs occurs in both fall and winter, but is observed only in winter in the GFS-based simulations. TIDI values peak in the fall in both downscaled runs, with inputs from the ERA5- and FNL-WRF datasets, but the extent of high TIDI values to the southeast of Qatar in fall is much larger in the ERA5-WRF run. This is also ~~true~~the case when comparing the FNL-WRF and FNL-based simulations. The differences have resulted in TIDI values varying by a factor of 2 to 10 in the south of the area of interest between ensemble members.

To further examine these results, the spatial distribution of the full-year median of the 96-hour integrated ^{131}I concentrations, converted to TIDI, and the full-year median of the air parcel ages coinciding with the maximum concentration of ^{131}I are shown in Figure 8. As expected, the age of the Lagrangian particles decreases southward with ~~the decreasing distance from~~proximity to the source. A~~We see that a~~ll ensemble members simulate~~ the age of~~ particles ages l~~ess~~ower than 25 hours along with relatively high levels of TIDI (^{131}I concentrations) at the southeastern edge~~corner~~ of the study area. The longer-lived particles (above 35 hours) are found in northern latitudes~~Qatar~~. In simulations based on the FNL dataset, particle ages in northern Qatar exceed 40 to 50 hours, while ~~falling below~~they do n'ot exceed 40 hours in ~~simulations from~~ other ensemble members. Furthermore, we ~~observe~~ obtain the larger extent of relatively higher TIDI to central Qatar in these simulations ~~compared to simulations from other ensemble members~~ (the~~se~~ ~~both~~ seasonal and ~~full-~~yearly median of TIDI is shown in Figures 6 and 8).

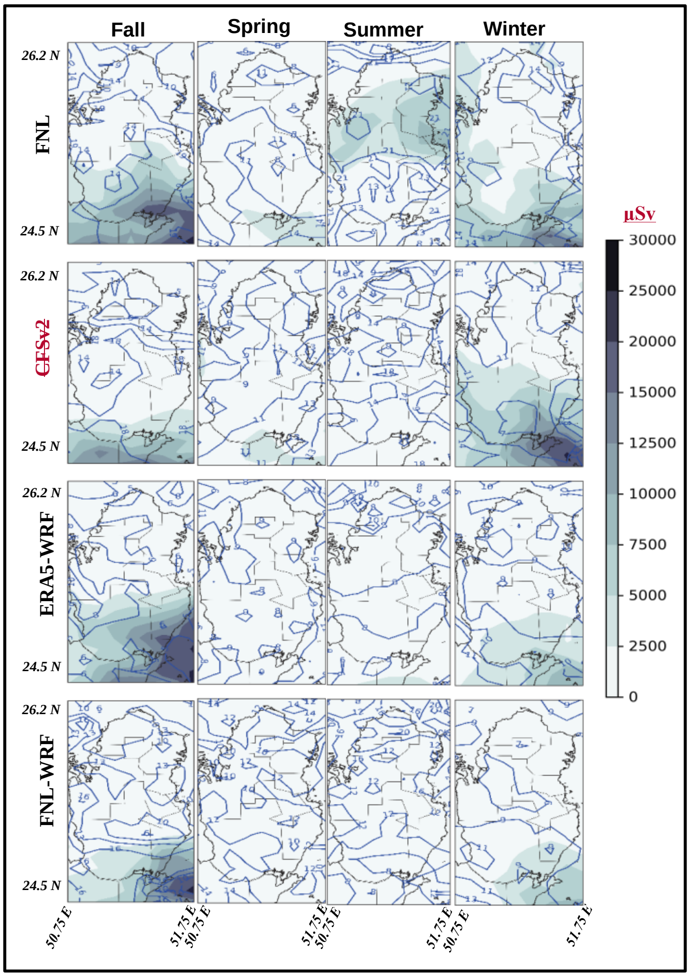

Figure 6 ~~the color scale shows the~~ S~~s~~easonal median of 96-hour integrated ^{131}I concentrations ($^{131}I^{intg_conc_seas}$) converted to thyroid internal dose from inhalation (TIDI, in units of μSv) for the adult age group. The contour lines (in local time, ~~the unit of~~ hours of the day~~in local time~~) depict~~are~~ the seasonal median of the Lagrangian particle release time coinciding with the maximum $^{131}I^{intg\_conc\_seas}$ found in each 96-hour run.

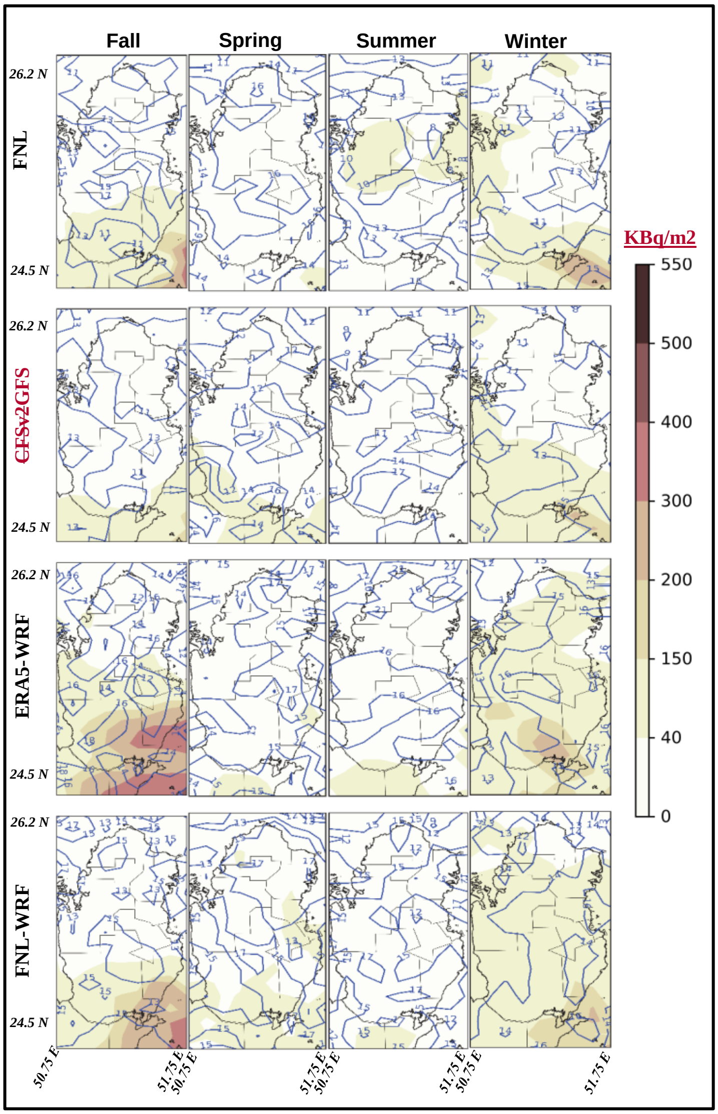
Fall
Spring
Summer
Winter
FNL
~~CFSv2~~GFS
ERA5-WRF
FNL-WRF
26.2 N
24.5 N
50.75 E
51.75 E
KBq/m2
550
500
400
300
200
150
40
0

Figure 7 Same as 6, but for the seasonal median total ^{137}Cs deposition ($^{137}Cs^{tot_depos_seas}$) in the units of Bqm^{-2}. The contour lines are the seasonal median Lagrangian particle release time coinciding with the completion of ^{137}Cs deposition found in each 96-hour run.

I~~From the above two points, i~~t can be concluded that a higher number~~frequency~~ of air parcels reach~~ing~~ areas away from the source (and not a lower ~~decrease~~ in transport speed~~speed to the same receptors~~) which ~~seems to cause~~leads to the abundance of longer-lived particles in FNL-based simulations. ~~Because of the high importance of the population being exposed to radionuclides,~~ TIDI and $^{137}Cs^{tot\_depos\_seas}$ are analyzed against the population density of Qatar (Fig. 9). ~~The spatial distribution of the population shows that t~~The desert areas of southern and southeastern Qatar, over which~~as the area of entry of~~ radionuclides en~~ne~~ter ~~in~~ the country~~region~~, host a small number of people or are almost uninhabited (Fig. 9-A). Figures 9-B and C show that the extremely high levels of TIDI (greater than 10000 µSv) and $^{137}Cs^{tot\_depos\_seas}$ (greater than 150 kBqm^{-2}) occur mostly in areas with a population density of less than five persons per arc-second. In the populated areas (with a density of more than 8 persons per arc second) the TIDI and $^{137}Cs^{tot\_depos\_seas}$ do not exceed ~~more than~~ 5000 µSv and 100 kBqm^{-2} in most cases. Due to the exceptional weather pattern that occurs in the simulations based on the FNL dataset in the eastern part of Qatar (where the most densely populated areas are located) in summer, the highest values of TIDI in densely populated areas are observed ~~in these simulations~~. Otherwise, all ensemble members simulate the highest TIDI during the cold seasons. ~~This is agreement with the previous results~~. The highest $^{137}Cs^{tot\_depos\_seas}$ in the same areas are observed ~~in the simulations of two members~~ based on ~~the~~ ERA5 and FNL-WRF ~~datasets~~ in the cold period of the year.

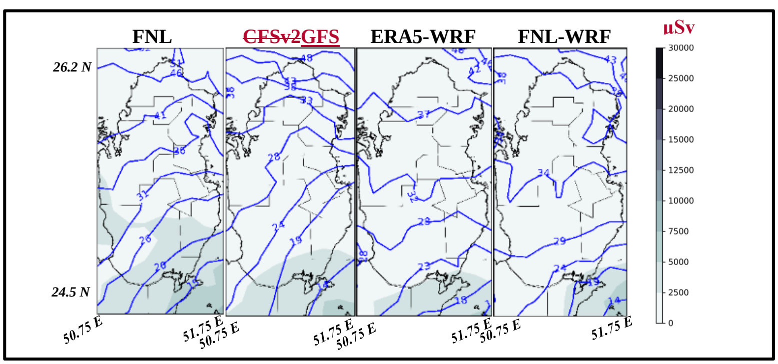

Figure 8 A: ~~t~~The full-year median TIDI (µSv) for the adult age group and B: The full-year median $^{137}Cs^{tot\_depos\_seas}$ (kBqm^{-2}). The contour lines are the full-year median age spectra coinciding with the maximum $^{131}I^{intg\_conc\_seas}$ and the completion of ^{137}Cs deposition found in each 96-hour run.

Formatted: Superscript

Formatted: Superscript

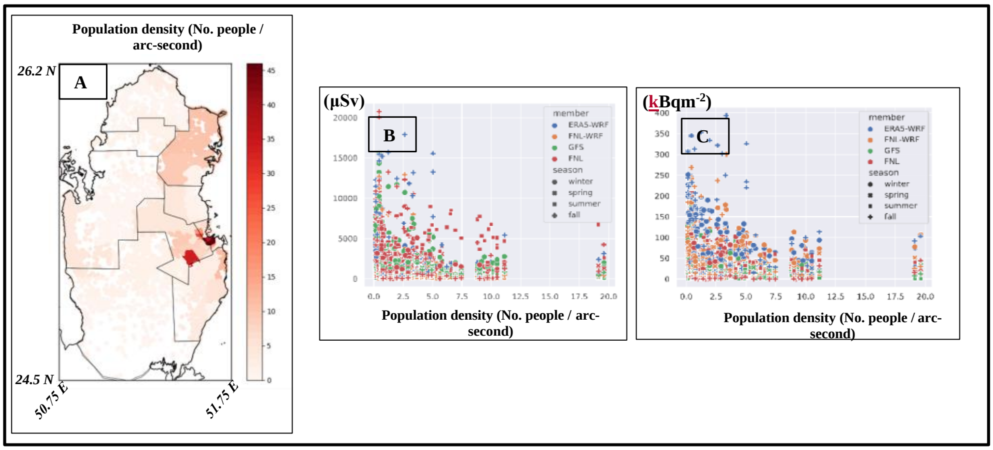

Figure 9 A: T~~the subplot A shows t~~he gridded population density of Qatar at one arc-second resolution in 2020. The relationship between TIDI (µSv) for the adult age group and $^{137}Cs^{tot\_depos\_seas}$ and the population density of Qatar are shown in B and C, respectively. The shapes and colors of the markers represent seasons and ensemble members.

In addition to the magnitude of the transported radioactive materials, the temporal distribution of the extreme events in the affected area is also of importance for ~~the~~ preparedness programs. Figure 10-A shows the frequency of occurrence (FoO) of ^{131}I concentrations above the 66th percentile. In all~~ the~~ members of the ensemble, more than half of the~~-~~ events~~events in most parts of Qatar~~, especially in the northern part, take place in the winter. While the FoO of high ^{131}I varies between around 15 and 30% in spring, the lowest FoO is observed in the summer when less than about 10% of the extreme events occur~~ in Qatar15% of extreme events have reached receptors in Qatar~~. The seasonal FoO of ^{137}Cs ~~column densities~~ concentrations (S9) also show ~~highly~~very similar~~s almost identical~~ results. A case where ERA5-WRF simulated the northwestward movement of the near-surface ^{131}I concentrations (Bq/m3) in~~on 14~~ January at noon is shown in the upper panel of Figure 10-B. We ~~have observed~~find a similar pattern in a large number of events in which high levels of radionuclides are transported to Qatar. This synoptic pattern ~~seems to be due~~is related to the juxtaposition of low and high-pressure cells located to the west and east of the region. The resulting pressure gradient cause strong south/southeasterly winds to develop between two cyclonic and anti-cyclonic cells, bringing the dense ^{131}I clouds into the study area. This pattern ~~occurs~~ mainly occurs in the late winter and early spring, coinciding with the southward movement of the westerlies and the eastward movement of the Saudi Arabian subtropical high pressure system ~~occurs mainly in the late winter-early spring period simultaneous with the southward movement of westerlies and the eastward movement of the Saudi Arabian subtropical high pressure~~ (De Vries et al., 2016). The lower panel of Fig. 10-B shows the summertime mean of near-surface ^{131}I concentrations (Bq/m3), obtained from simulations based on the ERA5-WRF database. The near-surface atmospheric circulation is superimposed on these simulations. The seasonal pattern found here illustrates well why very few extreme events are observed in the study area during the summer. The northwest-southeast winds, known as the Shamal winds (Yu et al., 2016), cause the simulated radionuclides to move away from the study area. Therefore, the highest (lowest) contamination risk to the population of Qatar from the occurrence of a nuclear accident and the resulting release of radionuclides is expected to occur in winter (summer).

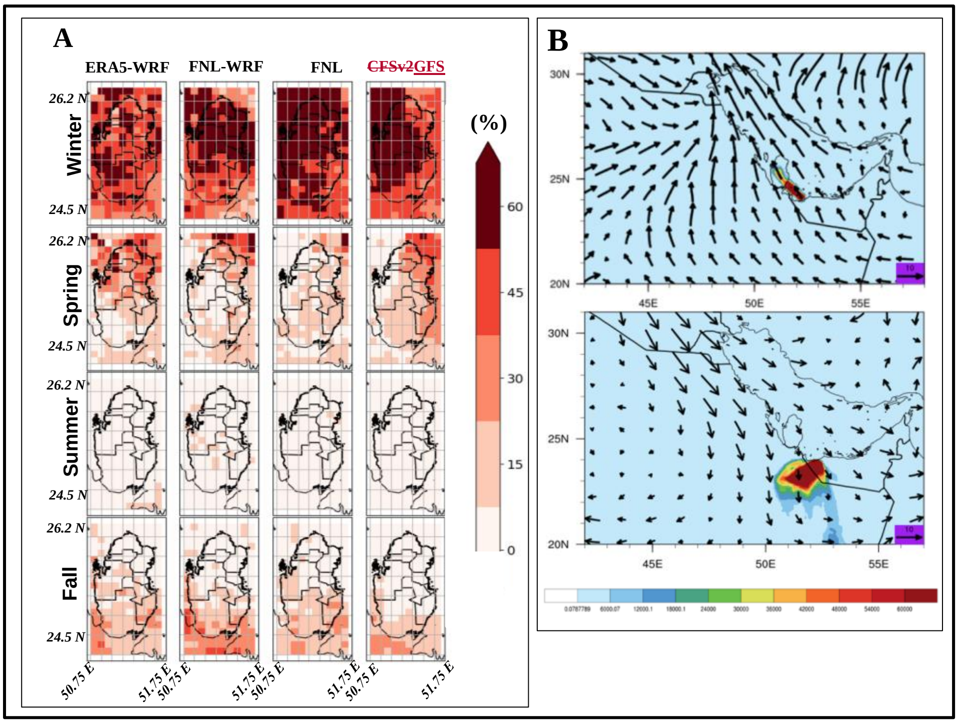

Figure 10 A: Frequency of occurrence (%) of ^{131}I ~~column densities~~ concentrations above the respective 66th percentile. B: The figure at the top shows the simulation of near-surface ^{131}I concentrations based on the ERA5-WRF dataset on January 14, 2019. The ~~, at noon (top) and the~~figure at the bottom is the summer average of near-surface ^{131}I concentrations. The wind field at 12:00 on the first day of the 96-hour simulation period is used to represent the atmospheric circulation during the radionuclide transport.

~~Concerning~~ With respect to the sensitivity of the radionuclide simulations to the choice of turbulence scheme, our~~the~~ results show~~s~~ that the use of STM leads to a more frequent occurrence of high ^{131}I concentrations and ^{137}Cs deposition within the

Commented [TCh2]: Define!

study area (Fig. 11). The difference between the seasonal (and full-year) median of the simulations in the STM- and GTM-based concentrations is trivial~~not noticeable~~. However, the upper quartiles of the simulations, especially in the cold seasons, show a significant increase after applying the STM scheme. The upper quartiles of the STM-based ^{131}I concentrations are 15.5, 16, and 21.2% higher than those of the GTM-based simulations in winter, fall, and year-round, respectively. The quartiles of STM-based deposition simulations also increase by 20, 20, and 12% over the same periods in comparison to GTM-based deposition simulations. The application of STM has comparable effects on concentration and deposition simulations based on the FNL-WRF dataset (shown in S10). The increase in ^{131}I concentrations and ^{137}Cs deposition values can perhaps be~~is~~ expected because under the skewed turbulence condition, downdrafts are more frequent than updrafts, resulting in higher surface concentrations and deposition in areas near pollution sources Pisso et al. (2019).

Commented [TCh3]: Need to define STM and GTM

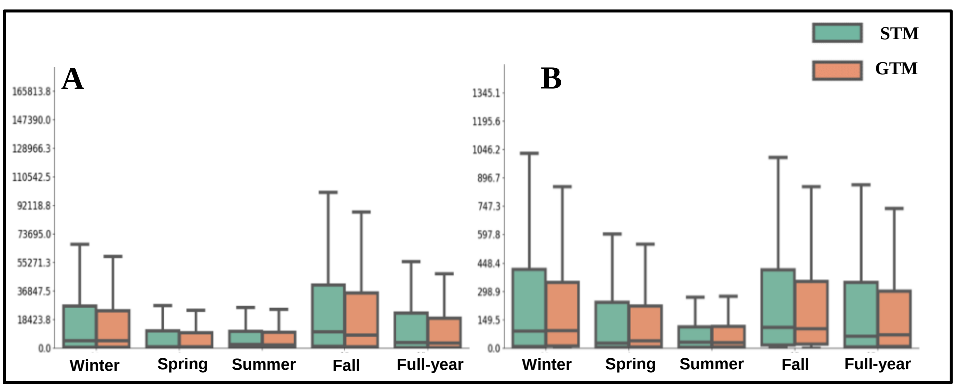

Figure 11 A: ~~and B show tThe box plot of the~~ 96-hour integrated simulations of ~~column densities of~~ ^{131}I concentrations (Bq/~~m2~~m3) from ERA5-WRF with STM (green, sensitivity run) and GTM (brown, control run), respectively. B: Same as A but for~~and~~ total deposition of ^{137}Cs (kBq/m2) ~~from ERA5-WRF with STM (green, sensitivity run) and GTM (brown, control run), respectively~~. The box borders show the quartiles of the simulations. The whiskers represent the range between 1.5 times the interquartile range above the upper quartile and below the lower quartile.

3.3 ~~Inter-comparison of FLEXPART and FLEXPART-WRF runs (~~effect of downscaling~~)~~

Radionuclide simulations based on (re)analysis datasets are assumed to be a better approximation of the actual ~~situation~~ atmospheric conditions than those based on the forecasting dataset (GFS, in this study) (Leadbetter et al., 2022). The ~~evaluation~~ statistical evaluation metrics used here are recommended by Maurer et al. (2018), who ~~searched for the best~~assessed transport models~~ to~~ simulating~~e~~ Xe-133 using measurements from six International Monitoring System (IMS) stations:~~. Among other evaluation metrics, they used~~ the fractional bias (FB) and the fraction within a factor of 5 (F5). FB, in the range -2 and 2, is the bias of the ~~simulation~~ simulated mean values normalized by the sum of the simulation and measurement means ~~by the sum of the two means~~ and multiplied by 2. F5 is the fraction of simulations that are at most one factor larger (5) or smaller (0.2) than the reference values. The Spearman correlation coefficient (r) calculated between the simulations of ^{131}I ~~column densities~~ concentrations shows that the ~~CFSv2 simulation~~GFS-based simulations are ~~well~~ closely associated with those of the (re)analysis-based members (red circles in the bottom row in Figure 12). The ~~CFSv2~~GFS-based simulations ~~have~~ attain the highest correlation with the FNL-based simulations (0.85) followed by FNL-WRF-based simulations (0.73). While the ~~CFSv2 simulation~~GFS-based simulations have (on average) a small~~trivial~~ FB (0.07) compared to the FNL-based simulations, they are positively biased compared to the simulations based on the FNL-WRF (-0.99) and ERA5-WRF (-0.98) datasets ~~(note that the placement of the (re)analysis members on the x-axis causes the FB to have a negative sign)~~. According to ~~FB5~~F5, 74.06% and 55.69% of the ~~CFSv2 simulation~~GFS-based simulations are ~~respectively~~ within a factor of 5 of the FNL and FNL-WRF-based simulations, respectively, whereas F5 decreases to 54.72% between the GFS- and ERA5-WRF-based simulations. The RMSE between simulations based on the ~~CFSv2~~GFS and FNL datasets (68443.95 Bq/m^3) is smaller than that found between the former and the FNL- (108001.33 Bq/m^3) and WRF-based (110632.06 Bq/m^3) simulations. As for the other~~with the previous~~ metrics, the ~~CFSv2 simulation~~GFS-based simulations produce the lowest and highest NMSE~~, the normalized RMSE which is less sensitive to extreme values,~~ against the FNL (1.24) and ERA5-WRF (8.78) simulations, respectively. In short, the GFS- and FNL-based simulations have the highest agreement due to the large~~significant~~ similarities between their meteorological inputs (~~see~~ subsection 3.1). Among all ensemble members, the largest difference ~~is~~ occurs between simulations based on ERA5-WRF and FNL datasets (r=0.55, FB=-0.92, ~~FB5~~F5=50.6%, RMSE=120282.62 Bq/m^3, and NMSE=11.18). ~~In contrast~~On the other hand, the downscaling of the inputs and the application of the same simulation code ~~lead to a~~yield closer higher agreement of the simulations based on the FNL-WRF and ERA5-WRF datasets than to those based on the FNL and FNL-WRF datasets (r=0.7 vs. 0.67, FB=0.01 vs. -0.93, ~~FB5~~F5=69.83% vs. 53.3%, RMSE=36012.82 Bq/m3 vs. 113888.80 Bq/m^3, and NMSE=2.74 vs. 10.08).

The evaluation metrics of~~calculated between the simulations of~~ ^{137}Cs ~~column densities~~ concentrations ~~show~~ lead to the same results as discussed above. For example, the simulations based on the GFS dataset ~~have~~ show the highest agreement with the FNL-based simulations (r=0.85, FB=0.07, ~~FB5~~F5=74.98%, RMSE= 8485.22 Bq/m^3, and NMSE=1.19). Similarly, simulations based on FNL and ERA5-WRF datasets and simulations based on FNL-WRF and ERA5-WRF datasets have the lowest and highest agreement among the (re)analysis-based members. ~~According to the unitless~~ For all metrics, including r ~~(with an exception between GFS and ERA5-WRF based simulations)~~, FB, F5 and NMSE, the GFS based simulations ~~have~~ leads to close~~a higher~~ agreement with those based on the (re)analysis data sets when comparing the ^{137}Cs concentration simulations than the ^{131}I concentration simulations. The comparison of the simulated ^{137}Cs deposition ~~shows~~ yields ~~lower~~poorer~~a general decrease in the~~ agreement between all ensemble members (Fig. 13). The inconsistencies between wet deposition rates ~~simulations~~ are much more pronounced than ~~between~~ for dry deposition~~simulations~~. ~~This is to be expected as the~~ The

Formatted: Superscript
Formatted: Superscript
Formatted: Superscript
Formatted: Superscript
Formatted: Superscript
Formatted: Superscript

precipitation occurrence and rate and cloud water content, which are required to calculate wet deposition, ~~, are among the most error-prone meteorological fields to predict~~~~have~~are associated with a high degree of uncertai~~t~~nty, ~~in~~which add~~ition~~ng to the ~~existing~~ uncertainties in the deposition parameterisation~~formulation~~ (Gudiksen et al., 1988). ~~In addition~~Moreover, FLEXPART and FLEXPART-WRF use different scavenging schemes (see subsection 2.1). However, ~~as with~~similar to the simulated concentrations, ~~CFSv2~~GFS-based simulations of ^{137}Cs (dry/wet) deposition show ~~the greatest~~closest agreement with FNL-based simulations. We also ~~observe~~ find that the largest difference between the simulated dry deposition of ^{137}Cs from all ensemble members ~~is seen~~occurs between those forced by the FNL and ERA5-WRF datasets. ~~The higher~~ Better agreement between the simulations based on the FNL-WRF and ERA5-WRF datasets than between those based on the FNL and FNL-WRF datasets is also ~~the true~~obtained for the simulations of ^{137}Cs dry deposition, but not for the simulations of ^{137}Cs wet deposition. The above results also apply to the simulations of ^{131}I deposition (Fig. S11), except that in this study ^{131}I is assumed to be ~~in the~~ insoluble, remaining in the ~~a~~ gas~~eous~~ phase~~radionuclide~~ and~~that~~ ~~does~~ not ~~undergo~~ subject to wet deposition.

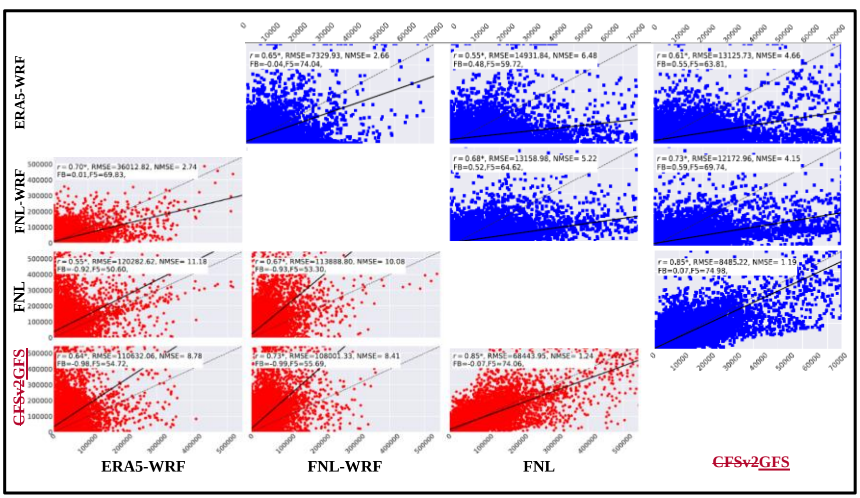

Figure 12 The inter-comparison of the 96-hour integrated simulations of near-surface ^{131}I (red circles) and ^{137}Cs (blue squares) ~~column densities~~ concentrations (Bq/~~m2~~m3) simulated at each grid point at each day of 2019. Solid and dotted lines show regression and identity lines, respectively. The asterisk next to the Spearman correlation coefficient (r) indicates a statistically significant correlation at $p<0.05$.

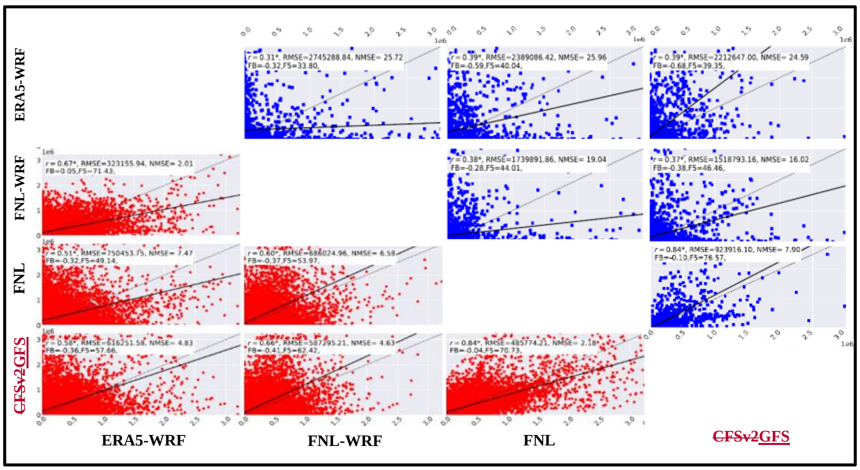

Figure 13 Same as Figure 12 but for ^{137}Cs dry (in red) and wet (in blue) deposition.

Conclusions

In this study, we examined the spatio-temporal dispersion of radionuclides, including ^{131}I and ^{137}Cs, in the ficticious event of ~~a~~ nuclear ~~accident~~accidents at the Barakah Nuclear Power Plant (B-NPP) in the United Arab Emirates (UAE). The resulting concentrations and deposition of the studied radionuclides ~~in the catchment region of interest (Qatar)~~we~~a~~re simulated using the Lagrangian particle dispersion model FLEXible PARTicle (FLEXPART) and FLEXPART coupled with the Weather Research and Forecasting model (FLEXPART-WRF). To investigate the diurnal and seasonal variations of the radionuclide dispersion, the particles (air parcels) wer~~ar~~e released within the first 24 hours of a 96-hour simulation period at B-NPP, between 100 and 300 m above ground level~~ (agl)~~, ~~with a daily iteration~~iterated daily over the year 2019. The source term is scaled to the maximum estimates of the radioactivity emissions~~e materials~~ from the Fukushima accident (22 PBq of ^{137}Cs and 192 PBq of ^{131}I)~~ to give the reader a tangible point of reference~~. ~~In the course of examining the study question,~~ W~~w~~e fou~~i~~nd~~pay special attention to the~~ differences in the simulations with respect to the meteorological inputs. We investigated the meteorological uncertainties by constructing an ensemble with three members based on (re)analysis datasets including Final Analysis (FNL) at native resolution, FNL and the ECMWF 5th Generation Reanalysis (ERA5) downscaled by WRF (ERA5- and FNL-WRF), and one member based on ~~the NCEP~~ the Global Forecast System ~~climate forecast system version 2~~ (~~CFSv2~~GFS) run by NCEP. This ensemble also providd~~es~~ the basis for comparing the simulations based on the forecast and (re)analysis datasets. The FNL- and GFS-simulations we~~a~~re compared with the simulations based on the FNL-WRF and ERA5-WRF datasets to determine the impact of downscaling and of using different/same model simulation codes (FLEXPART vs. FLEXPART-WRF) on the modeled dispersion. We also studied~~y~~ the sensitivity of ERA5- and FNL-WRF simulations to the turbulence scheme used under convective conditions. We compared the daily means of surface wind speed and temperature and daily total precipitation from the above datasets with observations measured from 157 ~~climate~~monitoring stations within the model domain. We examined the simulations of all four members in relation to Qatar's population density, with the goal of identifying possible risks to populated areas from a nuclear accident in the region. A summary of the results of the study is presented below:

1- **T~~he t~~ransport of radionuclides:** to analyze the time interval between emission and ~~observation~~ exposure to~~of~~ radionuclides, we investigated the age composition of the radionuclide plumes. Analysis of air parcel ages indicates that dense radionuclide clouds arrive in the south of the study area approximately 20 to 30 hours after the emission. A significant portion of ^{131}I released is transported to the most distant parts of the study area up to 40 to 50 hours after the ~~accident~~accidents. A~~In addition, a~~ll members simulated that a large fraction of the ^{137}Cs deposition occurs within the first 75 to 80 hours after the emission. The largest deposition of longer-lived~~r contribution of long-lived~~ particles wa~~i~~s found in FNL-based simulations for~~is found in~~ all seasons, except in the fall. We attribute~~d~~ this to the more distant transport of air parcels from the emission point in FNL-based simulations, compared to other members. The t~~T~~wo members which are forced by the downscaled datasets (FNL-WRF and ERA5-WRF)~~ and generated by the same simulation code (FLEXPART-WRF)~~ simulated a more similar distribution of air parcel ages than those simulated by the other two members~~ in all seasons except fall~~.

2- **D~~The d~~istribution of extremely high concentrations and deposition of radionuclides:** we calculated~~investigate~~ the seasonal median of 96-hour integrated ^{131}I concentrations ($^{131}I^{intg_conc_seas}$, ~~(~~in units of Bq m^{-3}), converted to the thyroid internal dose from inhalation ~~effective dose from inhalation of ^{131}I~~ (TIDI, in units of μSv), and the total ^{137}Cs deposition ($^{137}Cs^{tot_depos_seas}$) across the study area. As expected, all members simulated much higher TIDI over the south/southeast of Qatar, which is the closest point of the study area to the emission point~~, than over the more distant points in the northern half~~. The inter-seasonal comparison of the simulations showed~~s~~ that the ensemble members simulate the largest advance of TIDI > 2500μSv from the source to south/southeast of Qatar in the cold period of the year. The simulations of TIDI between the members of the ensemble differ by a factor of 10. In the simulations based on the FNL dataset, TIDI > 2500μSv cover the northern half of Qatar (in summer and fall) and the entire western half of Qatar (in winter). In the simulations based on the FNL-WRF dataset, TIDI > 2500μSv wa~~i~~s observed only over ~~the~~ southeastern~~ corner of~~ Qatar throughout the year. The differences in the TIDI simulations based on these two datasets demonstrated how the use of different model simulation codes and the downscaling of meteorological inputs can affect the FLEXPART modeling and, consequently, the decisions made based on its simulations after nuclear~~for real~~ accidents. Similarly, ~~there exist~~ remarkable differences were found in the spatio-temporal distribution of TIDI simulations based on the FNL and ~~CFSv2~~GFS datasets. This is the case even though these datasets are produced by the same base meteorological model~~ and are fed into the same simulation code (FLEXPART)~~. We attribute this to~~to~~

~~the fact that the~~ smalles~~t~~ differences in the meteorological inputs that lead to ~~sequential~~ cumulative deviations in the transport and concentration calculations of ~~air pollutants~~atmospheric contaminants. As with TIDI, $^{137}Cs^{tot\_depos\_seas}$ simulations from all the ensemble members peaked in the southeastern ~~corner~~ part of the study area in the cold period of the year when both wet and dry deposition occur. The ~~highest~~strongest ~~extent of~~ contaminat~~ed~~ion of areas ~~surfaces~~ with $^{137}Cs^{tot\_depos\_seas}$ greater than 40 kBqm^{-2} we ~~a~~re found in the simulations based on the ERA5-WRF and FNL-WRF datasets in winter. The highest levels of $^{137}Cs^{tot\_depos\_seas}$ (above 300 kBqm^{-2}) we~~a~~re found in the simulations based on the ERA5-WRF dataset in the southeastern corner of Qatar in the fall. This region received~~s~~ far less $^{137}Cs^{tot\_depos\_seas}$ (around 40 kBqm^{-2} and less) in the simulations based on the GFS and FNL datasets in the same period. The examination of the release time of the air parcels resulting in the extreme TIDI and $^{137}Cs^{tot\_depos\_seas}$ showed~~s~~ that the corresponding particles are mostly released between 9 a.m. and 2 p.m. LT. T~~It seems that t~~he development of the boundary layer height, the intensification of the thermal gradient between the land and sea, and the resulting onshore winds increase the transport of radionuclides to the study area during ~~at~~ this time of day. The analysis of the frequency with which ^{131}I and ^{137}Cs concentrations above the 66th percentile are transported to the populated areas of eastern Qatar showed~~s~~ that, for~~in~~ all members, more than 50% of the extreme cases occur in winter and between 15% and 30% in spring. The above results indicate that any nuclear accident ~~at B-NPP~~ in the winter will ~~be~~ more likely ~~to~~ be accompanied ~~by the~~with the highest radionuclide concentrations and deposition within the study area~~, especially in the southeastern corner of Qatar~~. This pronounced intra-annual variation~~distribution~~ is attributed to a seasonal atmospheric pattern in which south/southeasterly winds transport the dense radionuclide clouds ~~to the study area~~. The collocation of population density ~~and simulations~~ showed~~s~~ that the populated areas (with more than 8 persons per arc-second) receive~~coincide with~~ moderate (around 5000 µSv and 100 kBqm^{-2}) to low levels of TIDI and $^{137}Cs^{tot\_depos\_seas}$. Uninhabited areas in southern Qatar receive the highest levels of TIDI (above 10,000 µSv) and $^{137}Cs^{tot\_depos\_seas}$ (above 150 kBqm^{-2}). W~~In this study, w~~e also investigated the effect of the turbulence scheme selected under convective conditions on the radionuclide dispersion. The implementation of the Skewed Turbulence Model (STM) instead of the Gaussian Turbulence Model (GTM) increased~~s~~ the occurrence of high levels of ^{131}I concentrations and ^{137}Cs deposition. For example, the quartiles of simulations of ^{131}I concentration and ^{137}Cs deposition based on the ERA5-WRF dataset increased by 21~~.2~~% and 12%, respectively. According to Pisso et al. (2019), this can be interpreted as the enhancement of~~d~~ concentrations and deposition in the areas around the source under skewed turbulence conditions.

3- ~~The i~~**Inter-comparison of ensemble members:** the simulations of the ensemble members ~~are~~ have been compared~~, with a focus on the CFSv2GFS-based simulations~~. The simulations of ^{137}Cs and ^{131}I concentrations based on the GFS dataset we~~a~~re found to have the ~~best~~ closest agreement with the simulations based on the FNL dataset~~. CFSv2 simulation~~~~This is~~ because th~~e~~ey~~se input datasets~~ share a common meteorological base model. The comparison of wind speed, precipitation, and temperature from the GFS and FNL datasets showeds~~cause~~ the ~~highest~~ best agreement

Formatted: Superscript

Formatted: Superscript

Formatted: Superscript

Formatted: Superscript

Formatted: Superscript

compared to the other two input datasets. However, ~~the above results do not contradict~~we also fou~~i~~nd ~~the existence of~~ important~~significant~~ differences in the spatio-temporal distribution of GFS- and FNL-based simulations. This may be due to the ~~sequential~~ cumulative effect of ~~even small~~ ~~minute~~small differences in the meteorological inputs on particle dispersion. ~~In addition~~Further, ~~these~~ such differences may be caused by the inconsistency of meteorological parameters (~~,~~ which is beyond the scope of this study to examine) ~~all of them at different levels of the atmosphere~~. Our results showed that the sensitivity of the simulation to the meteorological inputs can be better represented by using both GFS and FNL datasets. The comparison of simulations based on ERA5- and FNL-WRF indicated ~~shows~~ that the downscaling of the inputs and the application of the same simulation increases the agreement of resulting simulations to an extent that exceeds the degree of similarity ~~agreement~~ between simulations based on FNL and FNL-WRF, with the same ~~origin~~ source of ~~the~~ meteorological inputs. The deposition simulations of all ~~the~~ members showed relatively ~~a~~ large~~r~~ inconsistency for both radionuclides. This wa~~i~~s more pronounced for the simulations of ^{137}Cs wet deposition. This is in part because wet deposition forcing factors are among the most ~~error-prone~~challenging meteorological ~~fields~~ parameters to model accurately~~predict~~. ~~In addition~~Moreover, the recently updated wet deposition scheme implemented in the FLEXPART uses different methods to determine the occurrence of wet deposition than FLEXPART-WRF (Girard et al., 2016, Gudiksen et al., 1988, Evangeliou et al., 2017).

~~3~~

Data availability. The FLEXPART and FLEXPART-WRF simulations are available upon request. The open-source codes for the FLEXPART 10.4 and FLEXPART-WRF 3.3.2 can be downloaded from https://www.flexpart.eu/downloads (last access: 27 May 2022). Qatar's high-resolution population density datasets are freely available at https://data.humdata.org/dataset/qatar-high-resolution-population-density-maps-demographic-estimates (last access: 27 May 2022).

Author contributions. SON performed the WRF, FLEXPART, and FLEXPART-WRF simulations and led the integration of results and writing. SON and TC designed the experiments. All the co-authors have read the paper and provided professional comments.

Competing interests. The authors declare that they have no conflict of interest.

Acknowledgments.

The CyI High-Performance Computing Facility and Qatar Environment and Energy Research Institute (QEERI) High-Performance Computer provided computational resources supporting this work. The authors thank the FLEXPART and FLEXPART-WRF developers for providing the transport model source codes.

Financial support.

This research has received funding from the Qatar Environment & Energy Research Institute (QEERI), an entity of the Hamad Bin Khalifa University, wholly owned by the Qatar Foundation for Science, Education, and Community Development.

Formatted: Normal, Indent: Before: 0.25", No bullets or numbering

References

ARNOLD, D., MAURER, C., WOTAWA, G., DRAXLER, R., SAITO, K. & SEIBERT, P. 2015. Influence of the meteorological input on the atmospheric transport modelling with FLEXPART of radionuclides from the Fukushima Daiichi nuclear accident. *Journal of environmental radioactivity,* 139**,** 212-225.

BABUKHINA, T., GAN'SHIN, A., ZHURAVLEV, R., LUK'YANOV, A. & MAKSYUTOV, S. S. 2016. Estimating by inverse modeling the release of radioactive substances (133 Xe, 131 I, and 137 Cs) into the atmosphere from Fukushima Daiichi nuclear disaster. *Russian Meteorology and Hydrology,* 41**,** 335-343.

BRIOUDE, J., ARNOLD, D., STOHL, A., CASSIANI, M., MORTON, D., SEIBERT, P., ANGEVINE, W., EVAN, S., DINGWELL, A. & FAST, J. D. 2013. The Lagrangian particle dispersion model FLEXPART-WRF version 3.1. *Geoscientific Model Development,* 6**,** 1889-1904.

CASSIANI, M., STOHL, A. & BRIOUDE, J. 2015. Lagrangian stochastic modelling of dispersion in the convective boundary layer with skewed turbulence conditions and a vertical density gradient: Formulation and implementation in the FLEXPART model. *Boundary-Layer Meteorology,* 154**,** 367-390.

CHINO, M., NAKAYAMA, H., NAGAI, H., TERADA, H., KATATA, G. & YAMAZAWA, H. 2011. Preliminary estimation of release amounts of 131I and 137Cs accidentally discharged from the Fukushima Daiichi nuclear power plant into the atmosphere. *Journal of nuclear science and technology,* 48**,** 1129-1134.

CHRISTOUDIAS, T. & LELIEVELD, J. 2013. Modelling the global atmospheric transport and deposition of radionuclides from the Fukushima Dai-ichi nuclear accident. *Atmospheric Chemistry and Physics,* 13**,** 1425-1438.

CHUNG, M. K. 2020. Gaussian kernel smoothing. *arXiv preprint arXiv:2007.09539*.

DE VRIES, A., FELDSTEIN, S. B., RIEMER, M., TYRLIS, E., SPRENGER, M., BAUMGART, M., FNAIS, M. & LELIEVELD, J. 2016. Dynamics of tropical–extratropical interactions and extreme precipitation events in Saudi Arabia in autumn, winter and spring. *Quarterly Journal of the Royal Meteorological Society,* 142**,** 1862-1880.

EVANGELIOU, N., HAMBURGER, T., COZIC, A., BALKANSKI, Y. & STOHL, A. 2017. Inverse modeling of the Chernobyl source term using atmospheric concentration and deposition measurements. *Atmospheric Chemistry and Physics,* 17**,** 8805-8824.

FARID, M., PRAWITO, SUSILA, I. & YUNIARTO, A. Design of early warning system for nuclear preparedness case study at Serpong. AIP Conference Proceedings, 2017. AIP Publishing LLC, 030067.

FAST, J. D. & EASTER, R. C. A Lagrangian particle dispersion model compatible with WRF. 7th Annual WRF User's Workshop, 2006. Citeseer, 19-22.

GALMARINI, S., BIANCONI, R., KLUG, W., MIKKELSEN, T., ADDIS, R., ANDRONOPOULOS, S., ASTRUP, P., BAKLANOV, A., BARTNIKI, J. & BARTZIS, J. 2004. Ensemble dispersion forecasting—Part I: concept, approach and indicators. *Atmospheric Environment,* 38**,** 4607-4617.

GIRARD, S., MALLET, V., KORSAKISSOK, I. & MATHIEU, A. 2016. Emulation and Sobol'sensitivity analysis of an atmospheric dispersion model applied to the Fukushima nuclear accident. *Journal of Geophysical Research: Atmospheres,* 121**,** 3484-3496.

GRELL, G. A., PECKHAM, S. E., SCHMITZ, R., MCKEEN, S. A., FROST, G., SKAMAROCK, W. C. & EDER, B. 2005. Fully coupled "online" chemistry within the WRF model. *Atmospheric Environment,* 39**,** 6957-6975.

GRYTHE, H., KRISTIANSEN, N. I., GROOT ZWAAFTINK, C. D., ECKHARDT, S., STRÖM, J., TUNVED, P., KREJCI, R. & STOHL, A. 2017. A new aerosol wet removal scheme for the Lagrangian particle model FLEXPART v10. *Geoscientific Model Development,* 10**,** 1447-1466.

GUDIKSEN, P., HARVEY, T. & LANGE, R. 1988. Chernobyl source term, atmospheric dispersion, and dose estimation. Lawrence Livermore National Lab., CA (USA).

HANNA, S. 1982. Applications in Air Pollution Modeling. Atmospheric Turbulence and Air Pollution Modeling. *Holland*.

HERSBACH, H., BELL, B., BERRISFORD, P., HIRAHARA, S., HORÁNYI, A., MUÑOZ-SABATER, J., NICOLAS, J., PEUBEY, C., RADU, R. & SCHEPERS, D. 2020. The ERA5 global reanalysis. *Quarterly Journal of the Royal Meteorological Society,* 146**,** 1999-2049.

IAEA 2009. *Regulations for the safe transport of radioactive material*, International Atomic Energy Agency.

JIN, D. Z. & KOZHEVNIKOV, A. A. 2011. A compact statistical model of the song syntax in Bengalese finch. *PLoS computational biology,* 7**,** e1001108.

KINASE, T., ADACHI, K., SEKIYAMA, T. T., KAJINO, M., ZAIZEN, Y. & IGARASHI, Y. 2020. Temporal variations of 90 Sr and 137 Cs in atmospheric depositions after the Fukushima Daiichi Nuclear Power Plant accident with long-term observations. *Scientific reports,* 10**,** 1-8.

LEADBETTER, S. J., JONES, A. R. & HORT, M. C. 2022. Assessing the value meteorological ensembles add to dispersion modelling using hypothetical releases. *Atmospheric Chemistry and Physics,* 22**,** 577-596.

LONG, P., HIEN, P. & QUANG, N. 2019. Atmospheric transport of 131I and 137Cs from Fukushima by the East Asian northeast monsoon. *Journal of environmental radioactivity,* 197**,** 74-80.

Formatted: English (United States)

Field Code Changed

Formatted: English (United States)

Formatted: English (United States)

Formatted: English (United States)

LUHAR, A. K., HIBBERD, M. F. & HURLEY, P. J. 1996. Comparison of closure schemes used to specify the velocity PDF in Lagrangian stochastic dispersion models for convective conditions. *Atmospheric Environment,* 30**,** 1407-1418.

MARYON, R. 1998. Determining cross-wind variance for low frequency wind meander. *Atmospheric Environment,* 32**,** 115-121.

MAURER, C., BARÉ, J., KUSMIERCZYK-MICHULEC, J., CRAWFORD, A., ESLINGER, P. W., SEIBERT, P., ORR, B., PHILIPP, A., ROSS, O. & GENEROSO, S. 2018. International challenge to model the long-range transport of radioxenon released from medical isotope production to six Comprehensive Nuclear-Test-Ban Treaty monitoring stations. *Journal of environmental radioactivity,* 192**,** 667-686.

MOUSSIOPOULOS, N. 1997. *Ambient air quality, pollutant dispersion and transport models*, European Environment Agency.

NABI, S. W., HAMEED, S. N. & VANDERBAUWHEDE, W. 2015. A Reconfigurable Vector Instruction Processor for Accelerating a Convection Parametrization Model on FPGAs. *arXiv preprint arXiv:1504.04586*.

NATIONAL RESEARCH COUNCIL 1999. Exposure of the American People to Iodine-131 from Nevada Nuclear-Bomb Tests: Review of the National Cancer Institute Report and Public Health Implications.

NCEP 2015a. National Centers for Environmental Prediction/National Weather Service/NOAA/U.S. Department of Commerce. 2015, updated daily. NCEP GFS 0.25 Degree Global Forecast Grids Historical Archive. Research Data Archive at the National Center for Atmospheric Research, Computational and Information Systems Laboratory. https://doi.org/10.5065/D65D8PWK. [Accesse 5th January 2023].

NCEP 2015b. NCEP GDAS/FNL 0.25 Degree Global Tropospheric Analyses and Forecast Grids. Research Data Archive at the National Center for Atmospheric Research, Computational and Information Systems Laboratory. https://doi.org/10.5065/D65Q4T4Z. [Accesse 5th January 2023].

PAPAGIANNOPOULOS, N., D'AMICO, G., GIALITAKI, A., AJTAI, N., ALADOS-ARBOLEDAS, L., AMODEO, A., AMIRIDIS, V., BAARS, H., BALIS, D. & BINIETOGLOU, I. 2020. An EARLINET early warning system for atmospheric aerosol aviation hazards. *Atmospheric Chemistry and Physics,* 20**,** 10775-10789.

PISSO, I., SOLLUM, E., GRYTHE, H., KRISTIANSEN, N. I., CASSIANI, M., ECKHARDT, S., ARNOLD, D., MORTON, D., THOMPSON, R. L. & GROOT ZWAAFTINK, C. D. 2019. The Lagrangian particle dispersion model FLEXPART version 10.4. *Geoscientific Model Development,* 12**,** 4955-4997.

SEIBERT, P. & ARNOLD, D. A quick fix for the wet deposition cloud mask in FLEXPART. EGU General Assembly Conference Abstracts, 2013. EGU2013-7922.

STOHL, A., FORSTER, C., FRANK, A., SEIBERT, P. & WOTAWA, G. 2005. The Lagrangian particle dispersion model FLEXPART version 6.2. *Atmospheric Chemistry and Physics,* 5**,** 2461-2474.

STOHL, A., HITTENBERGER, M. & WOTAWA, G. 1998. Validation of the Lagrangian particle dispersion model FLEXPART against large-scale tracer experiment data. *Atmospheric Environment,* 32**,** 4245-4264.

STOHL, A., SEIBERT, P., WOTAWA, G., ARNOLD, D., BURKHART, J. F., ECKHARDT, S., TAPIA, C., VARGAS, A. & YASUNARI, T. 2012. Xenon-133 and caesium-137 releases into the atmosphere from the Fukushima Dai-ichi nuclear power plant: determination of the source term, atmospheric dispersion, and deposition. *Atmospheric Chemistry and Physics,* 12**,** 2313-2343.

STOHL, A., SODEMANN, H., ECKHARDT, S., FRANK, A., SEIBERT, P., WOTAWA, G., MORTON, D., ARNOLD, D. & HARUSTAK, M. 2010. The Lagrangian particle dispersion model FLEXPART version 9.3. Tech. rep., Norwegian Institute of Air Research (NILU), Kjeller, Norway ….

TAKAGI, M., OHARA, T., GOTO, D., MORINO, Y., UCHIDA, J., SEKIYAMA, T. T., NAKAYAMA, S. F., EBIHARA, M., OURA, Y. & NAKAJIMA, T. 2020. Reassessment of early 131I inhalation doses by the Fukushima nuclear accident based on atmospheric 137Cs and 131I/137Cs observation data and multi-ensemble of atmospheric transport and deposition models. *Journal of Environmental Radioactivity,* 218**,** 106233.

TAPIADOR, F. J., ROCA, R., DEL GENIO, A., DEWITTE, B., PETERSEN, W. & ZHANG, F. 2019. Is precipitation a good metric for model performance? *Bulletin of the American Meteorological Society,* 100**,** 223-233.

THOMPSON, R. L., STOHL, A., ZHOU, L. X., DLUGOKENCKY, E., FUKUYAMA, Y., TOHJIMA, Y., KIM, S. Y., LEE, H., NISBET, E. G. & FISHER, R. E. 2015. Methane emissions in East Asia for 2000–2011 estimated using an atmospheric Bayesian inversion. *Journal of Geophysical Research: Atmospheres,* 120**,** 4352-4369.

TSURUTA, H., MORIGUCHI, Y. & NAKAJIMA, T. 2019. Dynamics of atmospheric 131 I in radioactive plumes in eastern Japan immediately after the Fukushima accident by analysing published data. *Scientific reports,* 9**,** 1-15.

UNSTATS 2020. *Demographic Yearbook 2020*.

WAI, K.-M., KRSTIC, D., NIKEZIC, D., LIN, T.-H. & PETER, K. 2020. External Cesium-137 doses to humans from soil influenced by the Fukushima and Chernobyl nuclear power plants accidents: A comparative study. *Scientific reports,* 10**,** 1-8.

WHO 2012. *Preliminary dose estimation from the nuclear accident after the 2011 Great East Japan Earthquake and Tsunami*, World Health Organization.

YU, Y., NOTARO, M., KALASHNIKOVA, O. V. & GARAY, M. J. 2016. Climatology of summer Shamal wind in the Middle East. *Journal of Geophysical Research: Atmospheres,* 121**,** 289-305.

Formatted: English (United States)

Field Code Changed

Formatted: English (United States)

Field Code Changed

Formatted: English (United States)

Formatted: English (United States)

ZHANG, Z. & CHEN, Q. 2007. Comparison of the Eulerian and Lagrangian methods for predicting particle transport in enclosed spaces. *Atmospheric environment*, 41**,** 5236-5248.